Laser Optoacoustic Imaging System for Molecular and Functional Imaging Research in Small Animal Models

by
Richard Su

A dissertation submitted to the Department of Engineering,
University of Houston
in partial fulfillment of the requirements for the degree of

Doctor of Philosophy

in Biomedical Engineering

Chair of Committee: Alexander Oraevsky

Co-Chair of Committee: Kirill Larin

Committee Member: Howard Gifford

Committee Member: Badri Roysam

Committee Member: Mini Das

Committee Member: Stanislav Emelianov

University of Houston
May 2021

ACKNOWLEDGEMENTS

I wish to express my deep gratitude to Prof. Kirill Larin and Prof. Alexander Oraevsky for their guidance of my research project. I would not have been able to accomplish this feat without their direction and support. I also would like to thank all the past and present employees of TomoWave Laboratories for their help that enabled me to learn and grow. Their advice and general knowledge has led me to be who I am as not only has it given me a large breadth of knowledge in the optoacoustic field but also life in general. Also I would like to acknowledge Dr. Mark Anastasio's lab for their support throughout the years with our advances in signal processing and algorithms of image reconstruction.

ABSTRACT

Optoacoustic tomography is an emerging field of medical imaging that is rapidly developing due to its unique capability to visualize and display molecular content of biological tissues with quantitative accuracy and excellent spatial resolution scalable with depth within live tissues. The main merit of optoacoustic tomography is in deep tissue imaging where resolution and contrast of pure optical imaging methods are limited by the strong optical scattering. The dominating tissue chromophores in the spectral range of laser wavelengths (650 nm to 1100 nm) that penetrate deep within tissues are hemoglobin and oxyhemoglobin of blood. Potential capability of functional optoacoustic tomography systems to measure concentrations of hemoglobin and oxyhemoglobin in humans provides for a variety of medical applications in the fields of diagnostics, therapeutic interventions and surgery. Using the methods of molecular imaging, it is also possible to visualize distribution of molecules that do not possess strong optical absorption in the near infrared spectral range, but can be targeted by special molecular and nano-particular contrast agents designed with strong optical absorption and high efficiency of acoustic wave emission through thermal expansion.

In spite of great promises the full potential of optoacoustic tomography in functional and molecular imaging has not been realized yet. In order to achieve capabilities of functional and molecular imaging, the optoacoustic tomography system has to overcome the tradeoff between high sensitivity of detection and ultrawide-bandwidth of ultrasonic frequency detection. Furthermore, quantitative imaging is only possible with knowledge of the optical fluence distribution through the entire volume of interest at each of the multiple

wavelengths of laser illumination. We took on a challenging task to develop such an advanced tomography system and enhance it with the methods of quantitative data analysis and image reconstruction. We designed and assembled a full view three-dimensional Laser Optoacoustic Imaging System (LOIS-3D) based on a 96-channel array of ultrawide band ultrasonic transducers and demonstrated its highest sensitivity to changes in the optical absorption coefficient $\delta \sim 0.03$/cm compared with any academic or industrial system. We proposed and implemented a signal processing method of transducer impulse response deconvolution that enabled reversal of distortions in the detected optoacoustic signals, which in turn allowed the experimental approach to functional and molecular imaging in live laboratory animals. The system technical specifications were characterized in a number of molecular imaging experiments. Finally, we proposed and implemented a practical method of the optical fluence normalization through the entire imaged volume based on measurements of the voxel brightness in blood vessels with known optical absorption and without computations of light propagation through tissues with unknown optical properties. We reconstructed previously unattainable functional images of the total hemoglobin and blood oxygen saturation in a volume of live tissue showing separately arteries, veins and tissues.

TABLE OF CONTENTS

ACKNOWLEDGEMENTS iii

ABSTRACT iv

LIST OF TABLES viii

LIST OF FIGURES ix

CHAPTER 1: INTRODUCTION **11**

1-1: Basic Principles of Optoacoustic Imaging 11

1-2: Significance of Quantitative Optoacoustic Imaging for Biomedicine 17

1-3: Current Status of Molecular Optoacoustic Imaging 19

CHAPTER 2: SYSTEM DESIGN AND PERFORMANCE **21**

2-1: Current Status of Optoacoustic Technology 21

2-2: LOIS-3D System Components and Parameters 22

2-2-1: LOIS-3D System Design 22

2-2-2: Laser 25

2-2-3: Fiberoptic Bundle 27

2-2-4: Amplifiers and Digital Acquisition Boards 29

2-2-5: Probe Parameters 32

2-2-6: Data Acquisition, Signal Processing, Reconstruction and visualization 35

2-3: LOIS-3D System Characterization 40

2-3-1: Resolution 40

2-3-2: Sensitivity 43

CHAPTER 3: APPLICATIONS IN ANATOMICAL IMAGING **51**

3-1: Mouse Body 51

3-2: Mouse Brain 54

CHAPTER 4: APPLICATIONS IN MOLECULAR IMAGING **55**

4-1: Biodistribution of Gold Nanorods 55

4-2: Tracking of Targeted IRDye-800 Tilmanocept 64

4-3: Conclusion 67

CHAPTER 5: TOWARDS FUNCTIONAL IMAGING **68**

5-1: Multi-spectral segmentation and co-registration 70

5-2: Fluence Normalization: Incident light on the skin, optical attenuation in-depth and between wavelengths 71

5-3: Functional images of [tHb] and [sO_2] 78

5-4: Conclusion 80

CHAPTER 6: CONCLUSION **82**

REFERENCES **84**

APPENDIX: SUMMARY OF SCIENTIFIC ACCOMPLISHMENTS **95**

LIST OF TABLES

Table 1: Comparison of features and parameters of deep tissue biomedical imaging modalities. 18
Table 2: Parameters of the laser illumination: Imaging module. 29
Table 3: Gain of the electronics system. Avg over 3 cycles (3, 10, and 17) and 3 input voltages ± StD 30
Table 4: Noise equivalent pressure calculations of the electronics system. Avg ± StD of 6 channels (40,43,48,49,54,57) for 2 input signals at 20, 25 and 40 MHz sampling rates. 32
Table 5: Transverse image resolution at 25 MHz sampling rate. Z slice – position of the horizontal slice with respect to the equator, Dist. From Ctr. Distance from the axis of rotation, Average – FWHM of an image, Std. Dev. – standard deviation. 43
Table 6: Transverse image resolution (central horizontal slice) at different sampling rates 43
Table 7: Statistics from the scan of a phantom that shows better even better sensitivity with more laser power as compared to the previous experiment 45
Table 8: Increase brightness in both mice post-IRdye800 injection 66
Table 9: Mean OAT aorta value from a single slice after laser fluence equalization at the individual wavelengths of 755 and 1064 nm. 1.6 multiplier was applied to the 1064nm wavelength based on the estimated absorption values of sO_2=100% sO_2 to achieve the expected ratio. 77
Table 10: Various arteries at different depths and heights 78

LIST OF FIGURES

Figure 1: Major components of the LOIS-3D system 23
Figure 2: (a) The LOIS-3D system with (b) the imaging module seen and (c) the orientation of the probe and fibers seen in a top-down view 25
Figure 3: Laser pulse energy measurements versus wavelength 27
Figure 4: The tool for measurement of the laser beam profile inside the imaging 29
Figure 5: System response to a 50 mV (50 dB attenuated) harmonic input at Ch 32. (a) 0.5 MHz, (b) 2 MHz, (c) 5 MHz. 30
Figure 6: Transducer 46 (a) noise without laser on (b) noise with laser on 31
Figure 7: Diagram of the ultra-broadband delta source used to measure the bandwidth of the LOIS-3D system 33
Figure 8: The delta source signal (a) and the resultant bandwidth from said signal 34
Figure 9: Signal and bandwidth of the LOIS-3D system from a broadband delta source 35
Figure 10: Images reconstructed from noiseless data function of μ_a by use of system matrices (a) Original, (b) spatial deconvolution, (c) electrical deconvolution, and (d) spatial and electrical deconvolution 37
Figure 11: Example of visualization done in 3D-Slicer from (a) raw image, (b) applied Scalar Opacity, (c) applied Scalar and Gradient Opacity and (d) after a few iteration of Scalar and Gradient Opacity manipulation and cropping of non-target voxels 40
Figure 12: Photograph of a hair phantom and the resultant 3D OAT reconstruction 41
Figure 13: Three cross-sections through the reconstruction of the hair phantom acquired at 25 MHz and with 0.02 mm voxel size. The vertical position of the slice is (a) -10 mm, (b) 0 mm, and (c) +10 mm to the center of the array probe. 42
Figure 14: Central horizontal sections of the hair phantom at different sampling frequencies: (a) 20 MHz, (b) 25 MHz, and (c) 40 MHz 42
Figure 15: An example of the image intensity profile through one of the hairs at the central horizontal section. 42
Figure 16: 1 mm thick slice through the phantom at 750 nm wavelength showing all tubes visible 45
Figure 17: Linear regression plot of the image brightness versus absorption coefficient of the tubes at a single wavelength, 750 nm 46
Figure 18: (a) OA image of two silicone tubes with GNR tube having a single knot (left) and MNP having two knots (right), both had an equal optical density of 1.0. (b) The average optoacoustic brightness Mean ± SD of the tubes with GNR and MNP. 48
Figure 19: Optoacoustic image brightness of MNP, showing linear dependence as a function of concentration with points on the graph corresponding to the optical density of 0.25, 0.5, and 1.0. 48
Figure 20: ICG (a) spectra for the two scanned wavelengths and the (b) linear trendline from the image brightness versus absorption after taking into account laser fluence. 50
Figure 21: Mouse scan with the (a) body being scan and (b) brain being scanned 52

Figure 22: Mouse body scans at 755 nm wavelength with different orientations of the mouse: (a) left side, (b) backside, and (c) right side 53
Figure 23: Mouse body scans at 1064 nm wavelength with different orientations of the mouse: (a) left side, (b) backside, and (c) right side 53
Figure 24: Mouse brain (a) OAT at 755 nm, (b) OAT at 1064 nm, and (c) atlas slice 54
Figure 25: Spectra of the GNR pre-PEGylation and post-PEGylation showing minimal changes to the absorbance spectra 56
Figure 26: 765 nm scan of one of the mice over the span of 8 days post-GNR injection 59
Figure 27: 1064 nm scan of one of the mice over the span of 8 days post-GNR injection 60
Figure 28: Trend of image brightness over time for the four regions of interest at (a) 755nm and (b) 1064nm 61
Figure 29: Samples of GNR intubated in blood outside of the mouse which can be seen to gradually broaden its absorption spectra over time 62
Figure 30: Mouse 1 (a) Pre- injection and (b) Post- injection 65
Figure 31: Mouse 2 (a) Pre- injection and (b) Post- injection 66
Figure 32: The aorta can be seen within the black square with the same coordinates at both (a) 755 nm and (b) 1064 nm. A multiplier was applied to the 1064 nm wavelength based on Roggan's expected ratio for 100% sO_2 at 755 and 1064 nm wavelengths. 71
Figure 33: Maximum voxel brightness (black) as a function of depth through the mouse with a voxel size of 0.1mm. Average estimated exponential curves of the optical fluence attenuation are in red for (a) 757 nm, measured μ_{eff}=1.26 cm^{-1} and (b) 1064 nm, measured μ_{eff}=0.97 cm^{-1}. 73
Figure 34: Maximum intensity projection of the mouse with 755 nm wavelength from (a) 3D OAT to (b) compensation of incident fluence on the skin to finally (c) compensation of incident fluence and in-depth through the mouse 74
Figure 35: Maximum intensity projection of the mouse with 1064 nm wavelength from (a) 3D OAT to (b) compensation of incident fluence on the skin to finally (c) compensation of incident fluence and in-depth through the mouse 75
Figure 36: Calibration of the 755 and 1064 nm wavelengths with (a) showing the 755 nm wavelength; (b) the 1064 nm wavelength with no multi-wavelength calibration; (c) the same 755 nm wavelength but in color; (d) the 1064 nm volume after wavelength calibration in color. 77
Figure 37: Total hemoglobin volume after optical fluence normalization through the volume of live tissue and voxel brightness normalization between wavelengths. (a) is the left side of the mouse, (b) is the backside of the mouse, and (c) is the right side of the mouse. 79
Figure 38: Functional optoacoustic imaging of the lower mouse body separating aorta and vena cava with intermediate blood oxygen saturation of yellow in-between. ... 79

CHAPTER 1: INTRODUCTION

1-1: Basic Principles of Optoacoustic Imaging

Optoacoustic (also known as photoacoustic) imaging is a method of image acquisition and reconstruction based on time-resolved detection of acoustic pressure profiles induced in tissue through absorption of short optical (laser) pulses. [1-4].

The spatial distribution of the optoacoustic pressure amplitude is defined as [5]

$$P(\vec{r}) = \mathrm{k}\,\Gamma(\vec{r})\,\mu_a(\vec{r},\lambda_i)F(\vec{r},\lambda_i) \quad (1)$$

where k is the system constant that remains the same in a given system, $\Gamma(\vec{r})$ is the Gruneisen parameter of the thermoacoustic efficiency, $\mu_a(\vec{r},\lambda_i)$ is the blood optical absorption coefficient at the wavelength λ_i, and $F(\vec{r},\lambda_i)$ is the optical fluence distribution at the wavelength λ_i.

In order to generate high-resolution volumetric optoacoustic images that display optical absorption properties of tissue, two conditions must be satisfied. The first, laser energy must be delivered to each voxel of tissue volume faster than resulting acoustic wave can escape from the voxel (the distance in tissue equal to the desirable spatial resolution), δ_s [6, 7]. For example, having desirable resolution of optoacoustic images of δ_s=150 μm, and the speed of sound propagation in tissue of $v_s = 1.5\ \mu m/ns$, one needs optical pulses significantly shorter than $\tau_L < 100\ ns$. The second, the detectors of acoustic waves (ultrasonic transducers) must be equally sensitive with an ultrawide band of ultrasonic frequencies. These types of acoustic detectors are called ultrawide-band ultrasonic transducers [6, 7]. The higher ultrasonic frequencies are responsible for spatial resolution of optoacoustic images, while the lower frequencies are responsible for volumetric contrast

of the tissue structures being visualized. Lack of sensitivity in the lower ultrasonic frequency range results in significant distortions in optoacoustic signals that cannot be reversed with signal processing. These distortions make only boundaries of volumetric objects visible on optoacoustic images, and reconstruction of quantitative optoacoustic images impossible. In order to relate tissue structures to optoacoustic images, the acoustic detectors must be capable of resolving not only rapid changes in optoacoustic signals associated with sharp edges and boundaries in tissues, but also reproduce slow changes associated with smooth variation in optical properties within relatively homogeneous tissue. An ultrawide-band ultrasonic transducer with equal sensitivity in the frequency range from about 100 kHz to about 10 MHz would be optimal for quantitative optoacoustic imaging in small animal models where the largest organs have characteristic dimensions of ~15 mm, while the spatial resolution of δ_s~0.15 mm allows visualization of smaller blood vessels and medically significant tissue structures.

Optoacoustic waves generated in each voxel of a volume of interest propagate as spherical acoustic waves. As a reasonable first approximation to the optoacoustic image reconstruction, one may consider biological tissues as an acoustically lossless homogeneous medium. In the case when pulsed laser illumination deposits thermal energy $H(\vec{r},t) = \mu_a(\vec{r})F(\vec{r},t)$ into the object of interest with distribution of the optical absorption coefficient, $\mu_a(\vec{r})$. It is convenient to consider optoacoustic wave equation in terms of the velocity potential, $\phi(\vec{r},t)$ [7]

$$(\nabla^2 - \frac{1}{c_0^2}\frac{\partial^2}{\partial t^2})\phi(\vec{r},t) = \frac{\beta}{\rho C_p} H(\vec{r},t) \qquad (2)$$

where $\phi(\vec{r},t)$ is related to the optoacoustic pressure through $p(\vec{r},t) = -\rho \frac{\partial \phi(\vec{r},t)}{\partial t}$. When the object of interest is part of acoustically, thermally and mechanically homogeneous medium, one can assume constant speed of sound, c_0, constant density, ρ, and constant thermoacoustic efficiency, Γ. The velocity potential for convenience can be replaced in Eq. (2) with temporal integral of acoustic pressure, $u(\vec{r},t)$ detected by transducer located in the point, $\vec{r}$, can be expressed in the following form [8]

$$u(\vec{r},t) = \int_{-\infty}^{t} p(\vec{r},t')dt' = \frac{\beta}{4\pi C_p} \int_V \frac{\mu_a(\vec{r}')I(\vec{r}')L(t - \frac{|\vec{r}-\vec{r}'|}{c_0})}{|\vec{r}-\vec{r}'|} d\vec{r}' \tag{3}$$

where $L(t)$ is the laser pulse temporal profile.

The integral in (3) is calculated over the entire space, V. It means that the acoustic pressure, $p(\vec{r},t)$ measured at the time, t and the point, $\vec{r}$ is determined by the acoustic sources located on the spherical shell with radius, $|\vec{r}-\vec{r}'|$ and thickness, $d\vec{r}'$. Acoustic waves arrive to the measurement point, $\vec{r}$ with time delay, $|\vec{r}-\vec{r}'|/c_0$. If the laser (illuminating) pulses are sufficiently shorter than the time of thermal expansion of each voxel (conditions of acoustic stress confinement are satisfied), then generation of thermal sources may be considered instantaneous and the laser pulse waveform function can be expressed in the form: $L(t) = \tau_L \delta(t)$, where τ_L is the laser pulse duration, $\delta(t)$ is Dirac's delta function. After these simplifications, the equation (3) can be rewritten the pressure, $p(\vec{r},t)$ recorded at transducer location, $\vec{r}$ can be expressed as a solution of Eq. (2) subject to initial $p(\vec{r},0) = \Gamma Q(\vec{r})$ and boundary $\left.\frac{\partial p(\vec{r},t)}{\partial t}\right|_{t=0} = 0$, conditions

$$p(\vec{r},t')\,dt' = \frac{\beta}{4\pi C_p}\int_V d^3\vec{r}\,' Q(\vec{r})\frac{d}{dt}\frac{\delta(t-\frac{|\vec{r}-\vec{r}'|}{c_0})}{|\vec{r}-\vec{r}'|} \qquad (4)$$

where $F(\vec{r})$ is the distribution of the laser fluence, and the non-negative function $Q(\vec{r}) = \mu_a(\vec{r})F(\vec{r})$ describes the spatial distribution of the absorbed optical energy in the acoustic sources.

The equation (4) can be considered fundamental for the optoacoustic tomography. The optoacoustic pressure amplitude detected by transducer at the time, t, is the superposition of the laser-induced acoustic sources located on the sphere of radius, $R = c_0 t$. The inverse problem in OAT is to determine an estimate of $Q(\vec{r})$ from knowledge of $p(\vec{r},t)$, i.e. the measured optoacoustic signal.

When a complete set of optoacoustic signal data can be acquired through entire 4π solid angle, the universal back-projection algorithm offers exact reconstruction of pressure, $p_0(\vec{r})$ in the acoustic sources for the planar, spherical and cylindrical geometries [8, 9]

$$p_0(\vec{r}) = \Gamma(\vec{r})\mu_a(\vec{r})F(\vec{r}) = \frac{2}{\Omega_0}\int_S d\Omega\left[p(\vec{r},t) - t\frac{\partial p(\vec{r},t)}{\partial t}\right]\Big|_{t=|\vec{r}-\vec{r}'|/c_0} \qquad (5)$$

where Ω_0 is the solid angle of the entire detection surface S with respect to a given source point at $\vec{r}'$, $p(\vec{r},t)$ is the pressure received at detecting position $\vec{r}$ and time t. Eq. (5) indicates that $p_0(\vec{r})$ can be obtained by back-projecting the filtered data function $\left[p(\vec{r},t) - t\frac{\partial p(\vec{r},t)}{\partial t}\right]$ onto concentric spherical surfaces centered at each ultrasonic transducer (see Fig.10). The magnitude of each data sample is then normalized to the factor, $Rd\Omega/\Omega_0$, which applies proper weight to voxels located at a distance, R, from the ultrasonic

transducers and visible within element aperture $d\Omega$ of each transducer relative to the total aperture of the array Ω_0.

Analytical reconstruction algorithms for optoacoustic tomography assume ideal ultrasonic transducers with full 2π wide directivity (ideal SIR) and delta function type EIR (equal sensitivity over entire range of ultrasonic frequencies). In the real world, however, the pressure waveform can be significantly distorted by the finite dimensions and the finite bandwidth of the ultrasonic transducers, causing artifacts on optoacoustic images. To compensate for transducer physical dimensions and electromechanical properties, iterative image reconstruction algorithms have been developed based on the transducer characteristics, which are described by time invariant linear systems with the transducer SIR and EIR as convolution kernels [9, 10]. As shown below, based on these imaging models, optoacoustic images can be reconstructed much more accurately. The iterative numerical methods provide quantitatively more accurate images at the expense of time required for image reconstruction. A comprehensive discussion of the state of the art in the optoacoustic image reconstruction can be found in [11, 12].

In order to acquire an accurate tomographic image using a rigorous reconstruction algorithm, the object of interest should be surrounded by transducers, so that the surface of detector positions is a closed surface. Otherwise, reconstruction will be made using incomplete set of data measurements, which is not quantitatively accurate [13]. Complete sets of temporary resolved optoacoustic data can be acquired using either two-dimensional arrays of transducers, or by one dimensional scanning of linear array of transducers or by two-dimensional scanning of a single transducer [14-16].

While optoacoustic images represent three-dimensional distribution of the opto-thermally induced pressure which is proportional to the absorbed optical energy, the ultimate goal of the optoacoustic tomography is to provide quantitative volumetric images of the optical absorption coefficient, which, in turn, is proportional to the concentrations of molecular chromophores. To convert optoacoustic images into quantitative molecular and functional images, one needs to normalize distribution of the optical fluence through the volume of interest by accounting for the optical attenuation. Optical attenuation in a highly scattering media which satisfies the diffusion theory can be characterized by the effective attenuation coefficient μ_{eff} (cm^{-1}) given as [17]

$$\mu_{eff} = \sqrt{3\mu_a(\mu_a + \mu'_s)} \qquad (6)$$

where μ_a and μ_s' are the optical absorption and the effective scattering coefficients respectively.

When generating quantitatively accurate optoacoustic images one has to account also for acoustic attenuation of ultrasonic waves. However, the main energy of optoacoustic waves resides in the lower ultrasonic frequency range (0.1 MHz - 3 MHz) where acoustic attenuation may be neglected compared to the strong optical attenuation.

The goal of our PhD project was to develop a system of three-dimensional quantitative optoacoustic tomography and a method of converting volumetric optoacoustic images into images of the optical absorption coefficient and then generate functional (molecular) images of the total hemoglobin and blood oxygen saturation. The greatest challenges of this project were associated with (i) development of an optoacoustic system capable of generating optoacoustic signals with high sensitivity and minimal distortions, so that reconstruction of quantitative optoacoustic images could be permitted and (ii)

development of a practical method applicable to live animals for normalization of the optical fluence based on experimentally measured voxel brightness, without computer models that rely on *a priori* unknown tissue optical properties.

1-2: Significance of Quantitative Optoacoustic Imaging for Biomedicine

Optoacoustic imaging came a long way from pioneering works describing basic principles [1-4] to demonstration of functional imaging in microscopy applications [18] to validation of its advantages compared to pure optical and pure ultrasound technologies in preclinical research [19-22] and clinical applications [23-26]. While entering the mainstream of medical imaging [27], optoacoustic tomography (OAT) is yet to deliver on its promise to provide quantitatively accurate functional and molecular images of live tissue volumes at clinically relevant depths of up to 50 mm. Therefore, extensive research continues in tissue phantoms and small animal models *in vivo* with the goal to develop a viable method of quantitative optoacoustic tomography (qOAT) [28].

Table 1 presents the most frequently utilized biomedical imaging modalities and their characteristics. Optoacoustic tomography is a molecular imaging technology since molecules (such as hemoglobin and oxyhemoglobin) absorb NIR light and produce optoacoustic signals. Distribution of molecules that do not absorb NIR light but have medical significance can be imaged using exogeneous contrast agents (dyes, nanoparticles).

Table 1: **Comparison of features and parameters of deep tissue biomedical imaging modalities.**

Imaging Modality	**X-ray CT**	**MRI MRT**	**Fluorescence BioLuminescence**	**Ultra Sound**	**Opto-Acoustic**
Excitation Energy	x-ray photons	RF waves in magnet	Optical NIR photons	Pressure waves	Optical NIR photons
Contrast Mechanism	Absorption by atoms in tissues	Relaxation time of H nuclear spin	Fluorophores Luminophores Nanoparticles	Density, speed of sound	HemoGb OxihemoGb Chromophores
Strength	whole body hard tissues	Whole body soft tissues	Molecular specificity Safe	Convenient Inexpensive soft tissue Safe	Quantitative Molecular specificity Safe
Weakness	Ionizing radiation Low specificity Toxic contrast	Expensive Low specificity Long scan Toxic contrast	Requires injection of contrast Medium depth Blurry in depth	Speckled contrast Boundaries only	Medium depth Complex tech
Resolution	High	High	Low	High	High
Contrast	Low	High	Medium	Low	High
Anatomical Functional Molecular	YES NO NO	YES YES NO	YES NO YES	YES NO NO	YES YES YES

The advantages of optoacoustic imaging are due to its ability to utilize the inherent advantages of both optical contrast and ultrasound resolution while not being limited by optical scattering and low mechanical contrast. While ultrasound imaging is capable of deep images that are centimeters in depth, it captures only mechanical properties and does not provide functional information. Optical imaging on the other hand offers the ability to visualize molecular content and cellular structures, but at the cost of imaging depth limited to submillimeter range. Optoacoustic imaging is able to leverage the strong optical absorption of blood found in the near-infrared (NIR) range of optical energy to help visualize vascular structures and hemodynamic responses while maintaining sub-millimeter resolution even after several centimeters in depth [1, 2, 7, 29]. X-ray based computed tomography is the most common method to detect disease but it uses ionizing radiation which can produce mutations and other damage to cells by oxidative stress, while the contrast and specificity of is low in soft tissues [30, 31]. Magnetic resonance imaging

uses non-ionizing radiation to provide images of fat, water, muscle and other soft tissues with high contrast. While it is also able to provide images of vasculature, it requires the use of toxic exogenous contrast agents and scans are often very time intensive [30, 32].

Biomedical imaging modality providing quantitatively accurate images with molecular specificity will result in breakthrough medical diagnostics and monitoring of therapeutical interventions. Specifically, quantitative functional images can provide pivotal medical diagnostic information about cancer angiogenesis, brain function, characterization of stroke and other vascular diseases.

1-3: Current Status of Molecular Optoacoustic Imaging

There are also a number of exogenous contrast agents being researched to enhance targets that do not have adequate absorption for optoacoustics especially when in the presence of strong endogenous background or deep imaging in general. There have been various investigations into getting the ideal balance of (1) high absorption per molar concentration; (2) a known sharp peak in order to be able to differentiate over background; (3) high photo stability to endure continuous scans of relevant light levels and (4) low toxicity [29]. These have led to the development of various nanoparticle contrast agents such as melanin [33, 34], carbon nanotubes [35, 36], gold nanoparticles [37-39] have been proposed contrast agents for optoacoustics.

There are also investigations into using commercially available fluorescent dyes such as indocyanine green, Alexa Fluor and IRDye [40, 41]. Here the advantages of fluorescence being able to provide single molecule sensitivity in superficial microscopic levels with the added benefits of optoacoustic providing deeper and better spatial resolution but needing a higher concentration of molecules [40].

Research into the contrast agent, delivery method used, in vivo kinetics, and biodistribution can be done with spectral decomposition. Spectral decomposition of two or more wavelengths which provide information on the exogenous and endogenous agents and kinetic studies are important to molecular imaging [29, 42].

CHAPTER 2: SYSTEM DESIGN AND PERFORMANCE

2-1: Current Status of Optoacoustic Technology

This phenomena was first discovered in 1880 by Alexander Graham Bell but recent advancements in ultrasound transducers, computers, and lasers has seen the field grown considerably [5, 42]. With the main chromphore in living animals being hemoglobin, it made optoacoustic well suited for imaging blood vessels and organs [7, 43-45]. Optoacoustic has gone many designs ranging from microscope systems developed by Maslov et al. [46] and Wang et al. [47], 3D optical interferometry system by Zhang et al. [48], and even 2D handheld that combined ultrasound and optoacoustic [49]. Various small animal pre-clinical systems have been studied and are even out in the market. iThera's MSOT inVision utilizes a ring array laser illumination and ultrasound detectors to produce real time cross-sectional images with a 10Hz frame rate and a spatial resolution of 150μm. VisualSonics Vevo systems incorporate a hand-held linear array to image mice.

A system requires three necessary pieces of equipment. The first requirement of a short-pulsed laser is due to the need of light to be delivered faster than the propagation of an acoustic wave through the distance of the tissue. That would mean for a possible resolution of 15 μm and a speed of sound of water of 1.5 μm/ns that the optical pulses would need to be shorter than 10ns and hence the reason for nanosecond lasers [7]. The second is an ultra-wideband ultrasound transducer as OA signals contain a wide frequency band generated from tissue from nanosecond lasers that can range from 0-100 MHz. Even considering that low frequencies are filtered for better visualization of smaller objects and that very high frequencies are attenuated greatly in tissue, there is still the possible 0.1-10

MHz which is close to 200% around its central frequency. In contrast, commercial ultrasound probes used in medical imaging have a relatively narrow band that is usually 50-80% around its central frequency due to the need to transmit and detect ultrasonic pulses [7]. The third is a data acquisition system that consists of analog amplifiers with high input impedance along with analog-to-digital converters in order to preserve wide band of ultrasound frequencies of OA [7].

Laser Optoacoustic Imaging System (LOIS) was custom designed with these design concepts in mind into a whole body 3D tomography system for the mouse with its merits lying in its ability to provide high contrast visualization of blood rich organs and vessels, functional images of blood concentration and oxygenation, and molecular information based on spectroscopy and exogenous contrast agents.

2-2: LOIS-3D System Components and Parameters

2-2-1: LOIS-3D System Design

The LOIS-3D system consists of the following components: imaging module, water circulation system, programmable logic devices, AC and DC voltage switches and relays, data acquisitions system, and power supplies. More details of the data acquisition boards, amplifiers, and laser fibers will be discussed in the following sub-chapters. A schematic of the LOIS-3D system with its components can be seen in Figure 1.

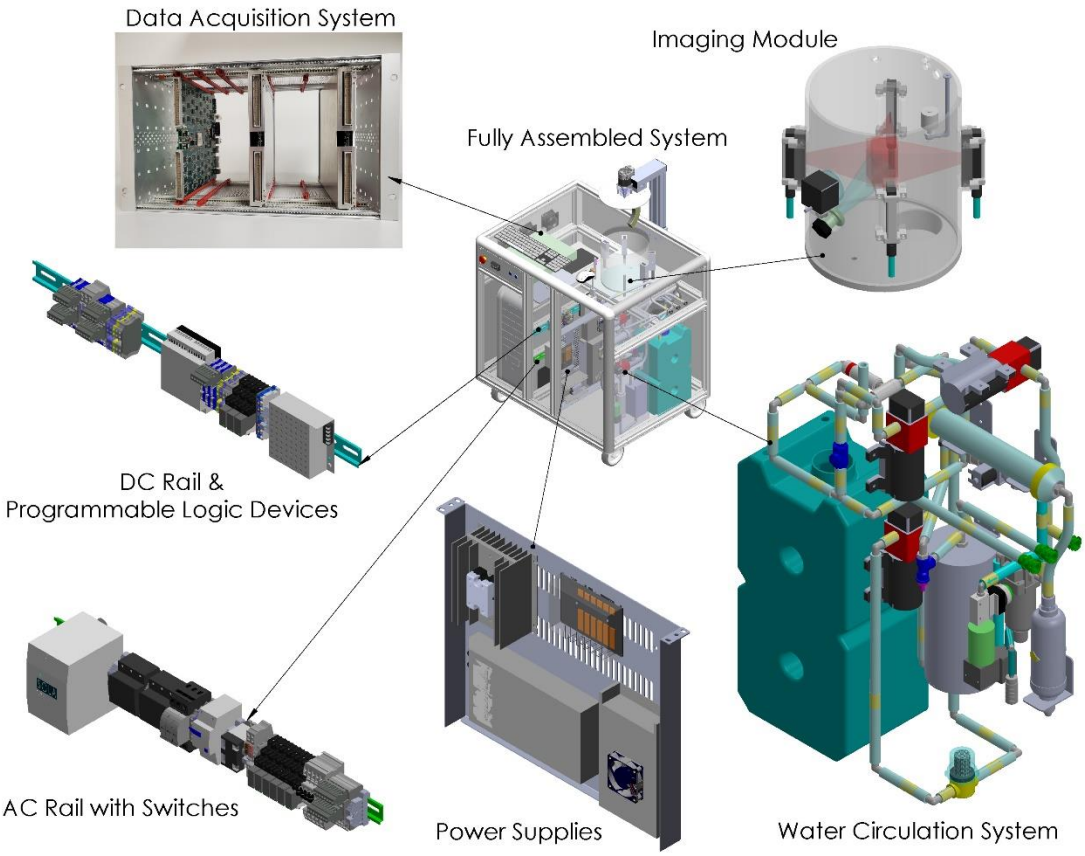

Figure 1: Major components of the LOIS-3D system

The imaging module contains the optoacoustic probe, motor, and fibers. The fibers are placed in orthogonal and backward mode (45° and 90° on each side of the probe). The target is placed onto the rotational motor along the axis of rotation where a scan has a static probe while the target rotates a full 360° for a full tomographic scan. Limitations on minimizing scan times correlate to the number of rotational steps per full scan and laser repetition rate (10 Hz). 320 rotational steps per scan were determined based on the probe's angular distance between transducers which correlated best with the specifications of the PSR-180UT Intellidrive motor (Philadelphia, PA). This would mean the minimum scan time would be under 40 seconds and averaging 12 acquisitions would increase this into the 7 to 8 minute range.

The imaging module containing the target and probe is filled with degassed distilled water and kept at a constant temperature of 36°C. Distilled water is pumped into a reservoir for storage until needed. Distilled water is then taken from the reservoir when experiments are to be done through a one-way channel, therefore preventing contamination backflow, into a circulation system that fills up the imaging module. This water circulation system contains a submersible 600 W water heater element attached to a proportional-integral-derivative controller that regulates and maintains water temperature at 36°C. This temperature was chosen as it is close to core body temperature and has an associated speed of sound of 1.522 mm/μs [50] which is comparable to the commonly used speed of sound of tissue used in ultrasound [51]. A degasser (3M Liqui-Cel, USA) is also within the circulation system to ensure a degassed state of the water during scans. It was observed that during the heating process of the circulation water, that bubbles would commonly form around the surfaces of the imaging module such as the probe and target but with the degasser, this was much less of a problem. Bubbles are a source of noise as they are acoustic scatters and may even provide a source of signal due to the water-air interface.

A camera is placed opposite of the probe so that the user can observe the placement of the target with respect to the probe and also observe the activity of the mouse. All these components are put inside the chassis and the imaging module itself is enclosed such that no stray laser light will leak out which can be seen in Figure 2a. Figure 2b shows the general orientation of the probe (2) and fibers (1). The top-down view seen in Figure 2c shows the target at the center of the axis of rotation with the two pairs of fibers in orthogonal and backward mode.

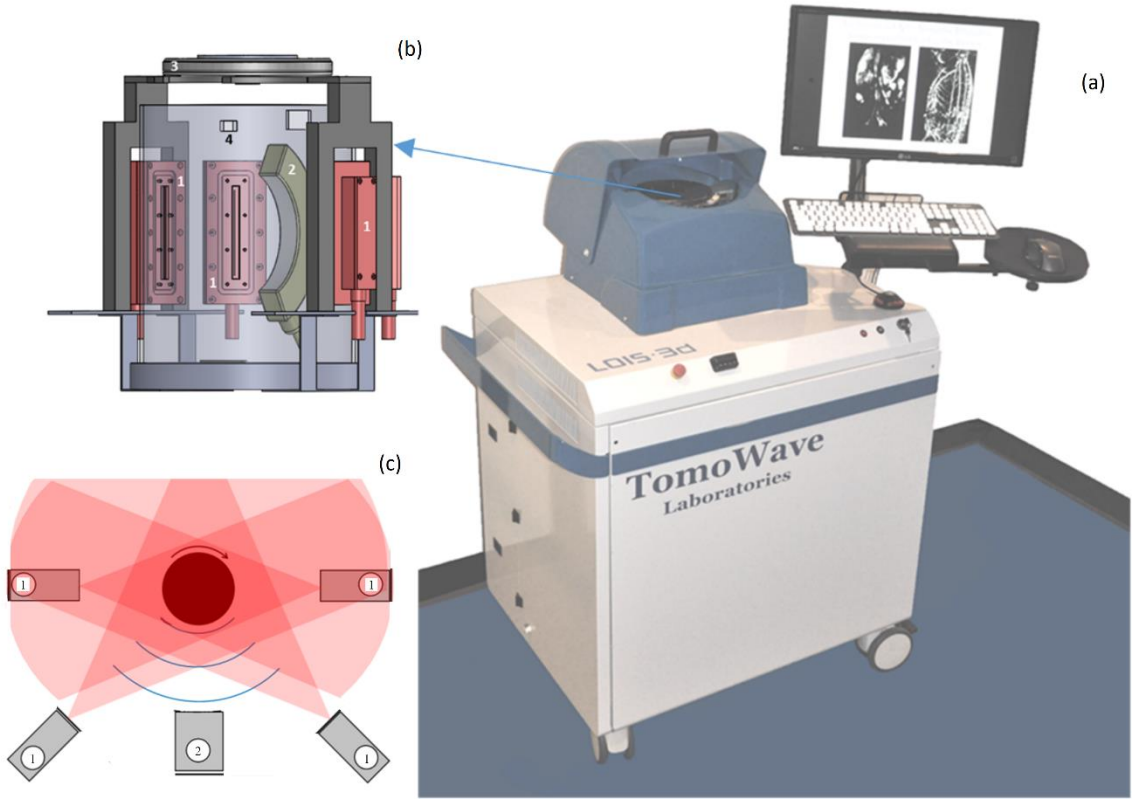

Figure 2: (a) The LOIS-3D system with (b) the imaging module seen and (c) the orientation of the probe and fibers seen in a top-down view

2-2-2: LASER

A custom-designed OPO-Nd:YAG laser for the LOIS-3D system is the PhotoSonus (Ekspla, Vilnius, Lithuania). It has a tunable range from 650 to 1064 nm with an output energy as high as 185 mJ with a 10 Hz repetition rate. The pulse duration is between 3 to 5 ns full-width-half-maximum (FWHM). For 1064 nm wavelength the laser could be as much as 610 mJ. The novelty of laser is due to its design that enables output of multiple wavelengths in a sequential interleaved manner (such as $\lambda 1 > \lambda 2 > \lambda 1 > \lambda 2$) to minimize

movement artifacts seen in-between wavelengths which were previously seen when doing one wavelength scan at a time.

The Photosonus wavelength settings were verified using an Ocean Optics USB4000 spectrophotometer with a P600-2-VIS-NIR optical fiber and associated Spectra Suite software from Ocean Optics. Scattered light from wavelengths of 757, 800, 840, and 1064 nm were checked to be correct when chosen and remained true when done in the interleaved modes. Additionally, the laser power was measured at the same four wavelengths with an Ophir PE503B-DIF-V2 smart head with a diffuser attached to the Ophir LaserStar interface. After five seconds of continuous laser-firing directly into the laser head, the averaged one-second interval was recorded and can be seen in Figure 3. Starting from 757 nm the measured pulse energy was around 168 mJ then at 800 nm it decreased to about 156 mJ and then further decreased to 152 mJ at 840 nm. Since 1064 nm is the pumping laser wavelength, it was measured to be 611 mJ.

The pulse width of the laser was checked using a Thorlabs DET10A/M photodiode connected to a Tektronix TDS3014 Oscilloscope. The oscilloscope was set to 50 ohm input load, DC coupling and to trigger off of a signal from the photodiode with a level of 1 V. The photodiode was held ~45° with respect to the emitted laser beam and the resultant laser pulse width was using full-width-half-maximum parameters.

1064nm 611mJ - measured at the output for the fiber coupling.

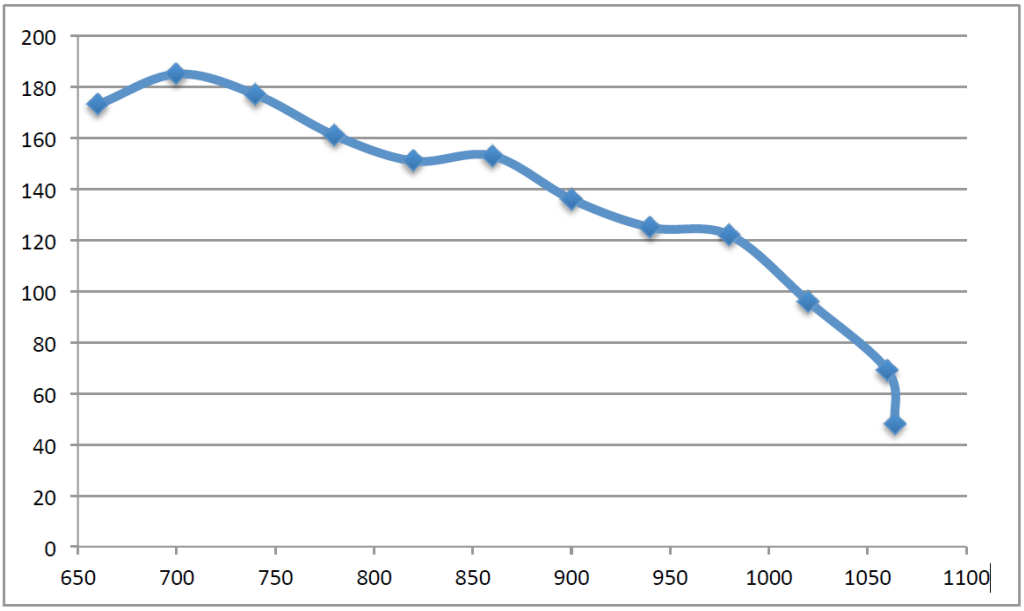

Figure 3: Laser pulse energy measurements versus wavelength

2-2-3: FIBEROPTIC BUNDLE

The laser output goes into a fiber bundle with the bundle's input aperature being a circle with a diameter of ~13 mm that splits into an output of four rectangles with dimensions of 2 mm by 20 mm. This beam expands further after passing through a ~85 mm water medium of the imaging module, an estimate of where the mouse would be located, to be about 25 mm by 30 mm. Transmission rate through the fiber bundle was done using the Ophir PE503B-DIF-V2 smart head with a diffuser and the Ophir LaserStar interface. Measurements were taken at 757 nm, 801 nm, 840 nm, and 1064 nm wavelengths. Laser energy was observed directly out of the laser and compared to measurements taken out of the fiber once attached to the laser. Additionally, laser beam size directly out of the laser and the area of illumination onto the smart head were recorded

to determine laser fluence, mJ/cm^2. The total transmission was about 50% and the results can be seen in more detail as part of Table 2.

To observe and measure the expansion of the beam from the fiberoptic illuminator, a grid with 1.5 mm resolution was printed on white paper and laminated to prevent it from getting wet. This grid was placed in the center of the imaging module to estimate the beam dimensions around the axis of rotation. This measurement tool can be seen in Figure 4. The 757 nm wavelength was chosen as it was easier to see with the naked eye. The ambient light was turned off and with the tool inside the imaging module full of water, estimates on the height and width were determined with the laser firing at 757 nm and used as the reference beam expansion for all tested wavelengths.

Average fiber fluence were calculations that took into account for the absorption of water through 9-10 cm layer between the fiberoptic output terminal and the center of the imaging module using the laser power head covered in thin, clear plastic to prevent water from seeping in. As the beam size would be within the power head aperture once aligned. The total laser power was then divided by the estimated beam area and the results can be seen as the averaged fiber fluence. In this maximum energy scenario when all beams converged, then the maximum energy at a mouse of 3 cm diameter would be around ~4.6 mJ/cm^2 which is still more than four times lower than the ANSI safety limit of 20 mJ/cm^2 [52].

Figure 4: The tool for measurement of the laser beam profile inside the imaging

Table 2: Parameters of the laser illumination: Imaging module.

Wavelength (nm)	**757**	**801**	**840**	**1064**
Laser output (mJ/pulse)	177.6	153.4	158.8	611
Combined fiber output (mJ/pulse)	87.9 ± 2.3	76.5 ± 2.3	76.2 ± 1.9	279.2 ± 2.2
Combined fiber transmission (%)	49.5	50	48	45.7
Average beam height (mm)	31 ± 2.0	N/A	N/A	N/A
Average beam width (mm)	26 ± 2.0	N/A	N/A	N/A
Average fiber fluence (mJ/cm^2)	1.15 ± 0.13	0.94 ± 0.10	0.91 ± 0.08	0.91 ± 0.00

2-2-4: AMPLIFIERS AND DIGITAL ACQUISITION BOARDS

Custom amplifiers and digital acquisition boards were designed and tested to ensure an ultra-wide broadband frequency range while maintaining good sensitivity and low noise. The electrical boards have a 1536 sample per acquisition with a sampling frequency range of 10 to 40 MHz and a maximum acquisition rate of 10Hz to coincide with available high-powered pulsed lasers. It is attached to a custom 96 channel probe from Imasonic (SAS, France).

Amplification was calculated based on injecting known sinusoids with different amplitudes from a Function Generator 3320A from Agilent (Santa Clara, Florida) into the electronic system. Three frequencies of 0.5, 2, and 5 MHz were selected to represent the range of the probe and tested with three different voltages of 10, 50 and 100 mV. Based on these studies, expected gains (G) ranged from 64dB to 66dB as seen in Table 3 with sample signals seen in Figure 5.

Table 3: Gain of the electronics system. Avg over 3 cycles (3, 10, and 17) and 3 input voltages ± StD

Frequency (MHz)	G @ 10mV (dB)	G @ 50mV (dB)	G @ 100mV (dB)	Gav (dB)
0.5	67.9 ± 0.6	64.9 ± 0.6	64.6 ± 0.1	65.8
2	65.8 ± 0.6	64.4 ± 0.3	64.5 ± 0.1	64.9
5	64.2 ± 2.3	63.8 ± 0.1	63.5 ± 0.1	63.7

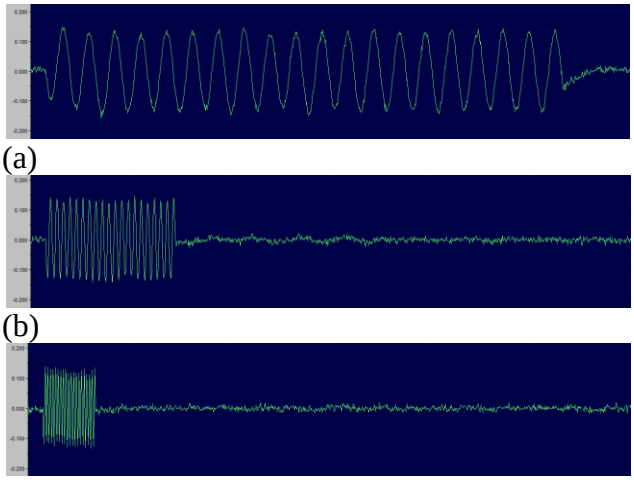

(a)

(b)

(c)

Figure 5: System response to a 50 mV (50 dB attenuated) harmonic input at Ch 32. (a) 0.5 MHz, (b) 2 MHz, (c) 5 MHz.

The noise was taken with all subsystems turned on (in-water probe attached to the electronics system, imaging module with water, water pumps circulating water, heater turned on, the motor turned on and the de-gassing system turned on) with only water in the imaging module. Three channels were chosen to represent the 96 channel system (22, 46, 90) and noise taken with and without a 1064nm wavelength pulse the laser. In Figure 6, the results show baseline noise taken at a 25 MHz sampling rate where one can observe the instance when the laser enters the imaging module and is seen due to the water-air interface around the 60 – 80 mm. Data was recorded at three different sampling rates with the associated Root Mean Square (RMS) noise value calculated to be 13.7 ± 2.1 mV for 20

MHz, 12.9 ± 2.1 mV for 25 MHz, and 11.3 ± 1.7mV for 40 MHz when the laser was firing at 1064 nm wavelength.

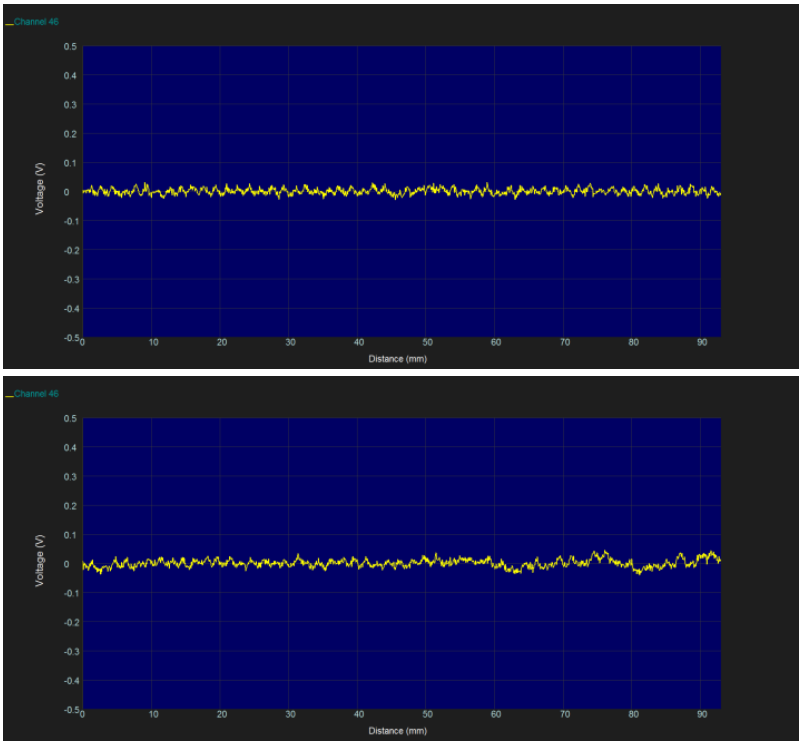

Figure 6: Transducer 46 (a) noise without laser on (b) noise with laser on

Sensitivity and noise equivalent pressure was determined using a calibrated DAPCO MB-6 hydrophone (Onda Corp., Sunnyvale, California) as an acoustic emitter with control handled by a Function Generator 3320A from Agilent (Santa Clara, Florida). Sine waves were set to be 2 and 2.5 MHz with 500mV peak-to-peak with a 20 burst cycle that corresponded to 70 Pa and 10 Hz repetition rate. The hydrophone was aligned vertically, horizontally, and rotationally to maximize the amplitude on channel 48. Data were acquired at 20, 25, and 40 MHz sampling rates with positive peak voltage by observing all the peaks and averaging within the middle cycles, and calculate the equivalent sensitivities. RMS noise was also calculated to find noise equivalent pressure but these tests did not involve any laser involvement. The overall sensitivity of the system was observed to be around 4.5

mV/Pa with the noise measured to be around 9mV which represents a noise equivalent pressure (NEP) around 2Pa. With averaging of signals, the noise can be further reduced which for example 16 averages would lower the RMS noise to around 2.5 mV or a NEP of 0.6Pa. You can see the results of the measurements of RMS and NEP in Table 4.

Table 4: Noise equivalent pressure calculations of the electronics system. Avg ± StD of 6 channels (40,43,48,49,54,57) for 2 input signals at 20, 25 and 40 MHz sampling rates.

No Averages				
Hydrophone Frequency, MHz	Sampling Frequency, MHz	Sensitivity, mV/Pa	RMNS, mV	Noise Equivalent Pressure, Pa
2.0	20	4.0 ± 1.0	9.0 ± 0.9	2.3 ± 0.5
	25	4.1 ± 1.2	9.3 ± 1.4	2.4 ± 0.6
	40	4.2 ± 1.2	9.0 ± 1.3	2.2 ± 0.4
2.5	20	4.5 ± 0.7	9.3 ± 1.3	2.1 ± 0.1
	25	4.7 ± 0.7	9.0 ± 1.4	1.9 ± 0.1
	40	4.7 ± 0.7	8.8 ± 1.4	1.9 ± 0.2
16 Averages				
Hydrophone Frequency, MHz	Sampling Frequency, MHz	Sensitivity, mV/Pa	RMNS, mV	Noise Equivalent Pressure, Pa
2.0	20	4.0 ± 1.1	2.9 ± 0.5	0.7 ± 0.1
	25	4.1 ± 1.1	2.6 ± 0.4	0.7 ± 0.1
	40	4.1 ± 1.2	2.4 ± 0.4	0.6 ± 0.2
2.5	20	4.4 ± 0.7	2.6 ± 0.3	0.6 ± 0.0
	25	4.6 ± 0.6	2.5 ± 0.4	0.6 ± 0.0
	40	4.7 ± 0.7	2.4 ± 0.4	0.5 ± 0.0

2-2-5: PROBE PARAMETERS

In order to characterize the receiver system of transducers and digital acquisition boards, a broadband delta source was created by using a short burst of light from a laser at 764 nm (output up to 65 mJ/pulse at 10Hz with an 8 ns pulse width) that hits a very thin and highly absorbing surface to create a pressure signal that is relatively flat over a very wide bandwidth. The laser was coupled with a 3/8 inch aperture fiber bundle (Dolan-Jenner Industries) where the output of the fiber a few millimeters from a biconcave lens of 12.7 mm diameter and a focal length of -15 to help expand the beam before the absorbing layer which was measured to have a final beam diameter of 40 mm. The absorbing layer was a

high-gloss black plastic paint (Krylon Fusion for Plastics) on a Rexolite plastic cylinder. The setup of this delta source can be seen in Figure 7.

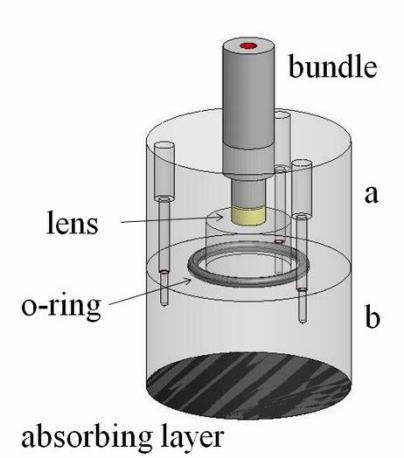

Figure 7: Diagram of the ultra-broadband delta source used to measure the bandwidth of the LOIS-3D system

Acoustic impulse signals were acquired from the delta source, which is shown in Figure 8, as sensed by the Onda GL 0200 calibrated hydrophone and following 17 dB amplification (SEA A17dB Hydrophone Preamplifier, 7.1 V/V into 50 ohm from 0.005 to 25 MHz). It is estimated that 30 mJ per pulse is propagated through the system under these conditions, and with the Onda hydrophone, our broadest band but least sensitive detector, we reliably observe a signal-to-noise ratio (SNR) over 50.

The impulse shown in Figure 6a is mono-polar and features minimal low-frequency overshoot (see broad structure around 700 ns). The full width at half maximum is 21 ns, which is more than twice the laser shot duration. It can be seen in Figure 8b, the -6 dB frequency roll-off occurs around 12 MHz, which is beyond the high-frequency roll-off of most common ultrasound probes and optoacoustic detectors. Further details into the specifications of the delta source are explained by Conjusteau [53].

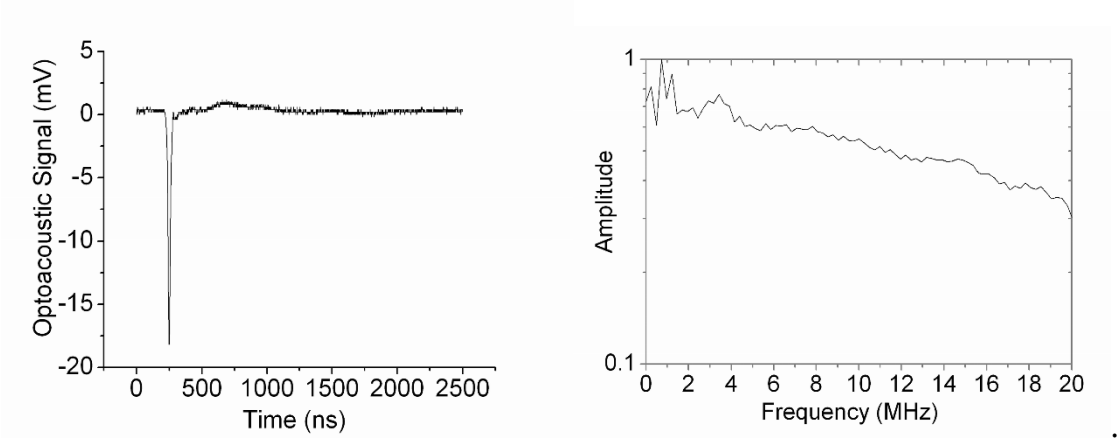

(a) (b)

Figure 8: The delta source signal (a) and the resultant bandwidth from said signal

The amplifiers and digital acquisition boards were attached to a 96 transducer arc probe of 1 x 1 mm elements with an arc angle that is a total of 113° (Imasonic, SAS, France). This receiver system was characterized using the delta source by maximizing the signal on the central channel of the probe, 48. The electrical impulse response was recorded off of this delta source and showed a bandwidth of the probe and system to be a -3dB of 0.15 to 6.5 MHz and -6dB bandwidth of 0.1 to 8.5 MHz. You can see the measured impulse response and the resultant bandwidth of the system in Figure 9.

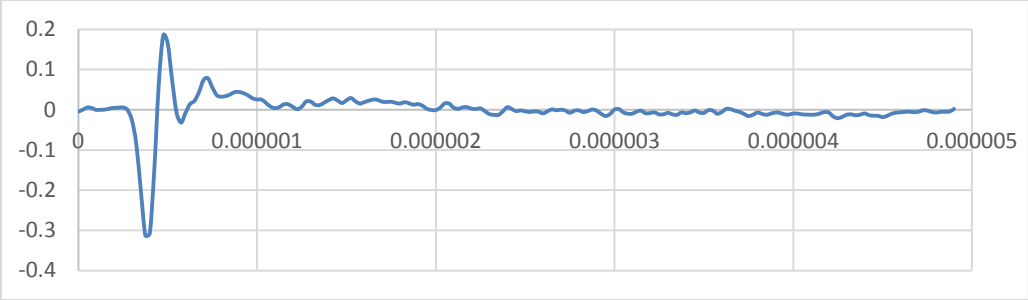

(a) Acousto-electric response at 40MHz sampling rate

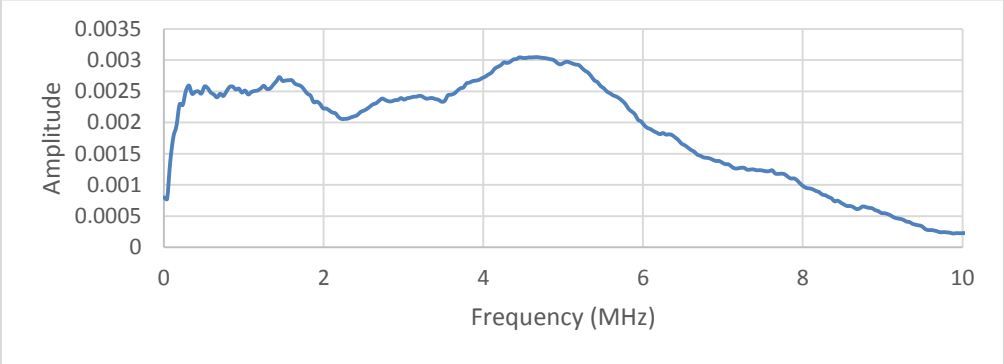

(b) Fast Fourier Transform for the bandwidth

Figure 9: Signal and bandwidth of the LOIS-3D system from a broadband delta source

2-2-6: DATA ACQUISITION, SIGNAL PROCESSING, RECONSTRUCTION AND VISUALIZATION

A standard imaging procedure typical of *in vivo* imaging was implemented with a standard protocol of signal processing, image reconstruction. The steps of this protocol include: (a) Acquisition and storage of RF optoacoustic signals (320 sets of signals corresponding to 320 rotational positions of the ultrasonic transducer array with 96 channels (b) Signal filtration using principal component analysis (PCA) on the first component present in all the channels [54]. This filter removes systemic noises and artifacts that appear on all electronic channels simultaneously, such as signals generated by the laser on the surface of transducers, or electromagnetic bursts that can be present in an imaging center facility, especially emitted by MRI machines. (c) Wiener deconvolution of the acousto-electrical impulse response [9]. This signal processing is aimed at correcting the

detected optoacoustic signals for limited bandwidth, especially in the range of lower ultrasonic frequencies. (d) Band-pass filtering of the optoacoustic signals especially helpful when the object of interest has one main dimension, such as diameter of hairs or tubes filled with optically absorbing aqueous solutions. (e) Image reconstruction using a modified universal back-projection algorithm [55], where modifications were aimed at a greater quantitative accuracy, involving deconvolution of the transducer spatial impulse response (SIR) and reversal of other distortions [11].

General signal processing took into consideration the bandwidth of the probe. Butterworth bandpass filters of 0.15 to 8 MHz were the most commonly used. With the help of the delta source, the acousto-electric impulse response was able to be recorded. This can be used in Wiener deconvolution for the restoration of the absorbed energy distribution from the system transfer function [9, 42, 56]. An investigation into the use of the Wiener deconvolution was done on a digital phantom which shows the spatial improvement when the physical response of the transducer is accounted for in Figure 10.

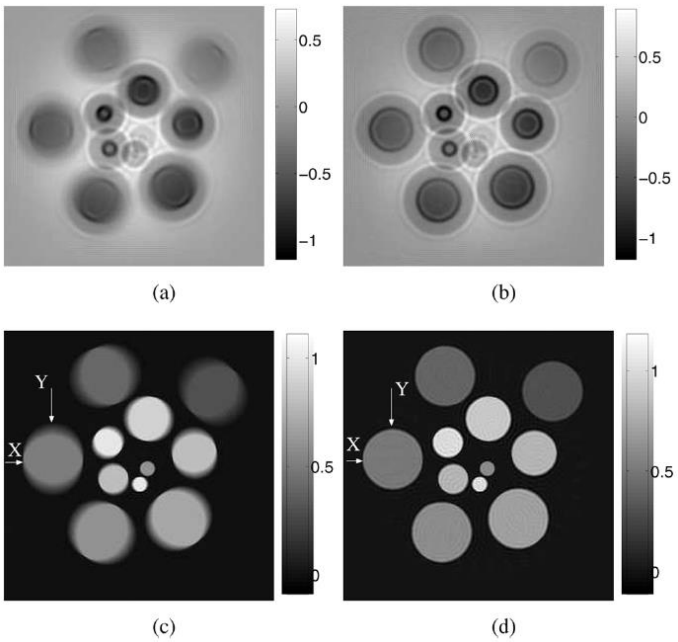

Figure 10: Images reconstructed from noiseless data function of μ_a by use of system matrices (a) Original, (b) spatial deconvolution, (c) electrical deconvolution, and (d) spatial and electrical deconvolution

Reconstructions are based on a universal filtered back-projection for a tomographic scan that would create a 30,720 sphere of virtual transducers around the target. Given the illumination area, a reconstruction of 25 x 25 x 30 mm with 0.1 mm voxels (total of 18,750,000 voxels) can be completed within one minute with the help of GPU parallel processing and the nVidia GTX 1080Ti graphics card that has 3584 CUDA cores. This can be further sped up with better graphics cards like the nVidia RTX 3060 but it was still much faster than earlier versions while still achieving good small animal body scans [9, 39, 57].

Iterative reconstructions were also investigated in collaboration with Dr. Mark Anastasio's group using the penalized least-squares method that used either the quadratic smoothness penalty (PLS-Q) or the total variation norm penalty (PLS-TV). These studies included tubes and mice and proved that PLS-TV was the better performing algorithm when there was incomplete data for 180 angular steps as opposed to 360. Currently, the

LOIS-3D system does not use iterative reconstruction as it is still considered too computationally intensive and it is thought that FBP reconstructions were sufficient as they were faster in terms of the time of reconstruction which would take minutes as opposed to iterative reconstructions that were studied at the time that took several hours for a single iteration and approximately 20 iterations would be needed before they could converge [11].

Three-dimensional optoacoustic images will first result in an opaque volume that needs to be processed to see what is relevant. In the case of a live mouse, the goal of image visualization is to make certain voxels transparent, so that tissue structures of interest are visualized while background tissues insignificant for biomedical research are transparent. Using LOIS-View (a software package developed by TomoWave based on 3D-Slicer (version 4.13.0) an open SDK source provided by Kitware (New York, USA). Visualization begins with the generation of the image histogram, i.e. by plotting the total number of voxels with specific brightness as a function of brightness. Then we create a Scalar Opacity Map (SOM) by making clear those voxels that belong to noise. To start the image visualization process, we set a threshold below which all voxels are clear. This way we remove all outlier voxels with negative brightness values because the presence of any negative values is a result of experimental noise in optoacoustic tomography system. A threshold value can be increased above 0 to remove noise in the background tissues with positive brightness. Application of a threshold is followed by a ramp of scalar opacity to make certain tissues semi-transparent. LOIS-View software allows one to take full advantage of the histogram and create nodes, i.e. turning points, thereby allowing full opacity to tissues with higher brightness and remove or reduce the visibility of tissues with lower voxel brightness. A node is a point on a histogram where the slope of scalar opacity

changes. This can be seen in Figure 11a (raw volume) to 11b (some Scalar Opacity Mapping applied). The next step is to apply the Gradient Opacity Map (GOM), which allows one to make boundaries sharper. A threshold also can be applied to the GOM to reduce noise but still maintain the brightness of the objects of interest. An example is seen in Figure 11c which had taken Figure 11b and now applied a Gradient Opacity Mapping. One may go back and forth between SOM and GOM until the volumetric image looks sharp and clear to present the blood circulation tree with continuous branching and organs identifiable by their shape and location on the anatomy atlas as a potential final result seen in Figure 11d.

Using the Color Opacity Map, one can use colors to replace specific grayscale brightness values. For example, it is beneficial to color arteries red and veins blue on functional images while tissue structures can be assigned yellow or other colors. Note that because hemoglobin of blood is the dominating chromophore for the NIR-I spectral range of light, anatomical optoacoustic images in NIR-I are made possible by different concentrations of blood in various organs and tissue structures. Even ribs, the vertebra of the spine, and joints are visible on optoacoustic images due to the presence of blood in the bones. It is possible, in principle, to assign different colors to different organs, if these organs have either different blood concentrations or different blood oxygen saturation.

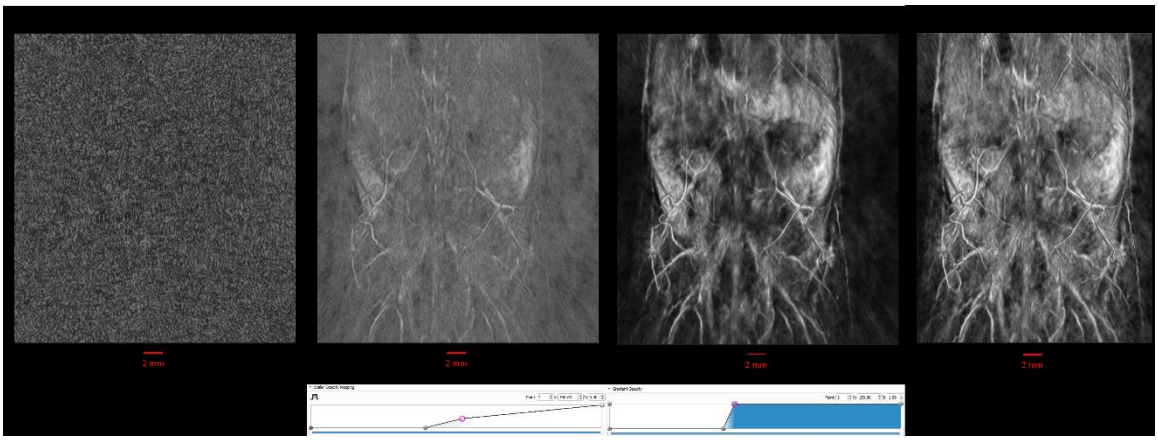

(a) (b) (c) (d)

Figure 11: Example of visualization done in 3D-Slicer from (a) raw image, (b) applied Scalar Opacity, (c) applied Scalar and Gradient Opacity and (d) after a few iteration of Scalar and Gradient Opacity manipulation and cropping of non-target voxels

When an image is acquired faster (without signal averaging) with visible outlier voxels, one can employ a median filter to remove such outliers. Within a window or kernel that includes the voxel in question, all the brightness values are sequentially ordered to determine the median (or middle) value of the sequence. This middle brightness value will become the new brightness value for the voxel in question (same x,y,z coordinates) in the newly created median filtered volume.

2-3: LOIS-3D System Characterization

2-3-1: RESOLUTION

A resolution test was based on a phantom with horse hairs with an average diameter of 0.12 mm. There were three total hairs with two crossing in an x formation and a third more vertical. A picture of the phantom can be seen with its corresponding 3D OAT reconstruction in Figure 12. A scan at 840 nm with 320 steps and 6 averages was taken at 20, 25, and 40 MHz sampling rates. Signal processing included principal component analysis (PCA) on the first component on all the channels and also on all the acquisitions

and Wiener deconvolution of the acousto-electric impulse response. The 3D reconstruction was then separated into 3 horizontal 2D slices equally spaced from -17 mm to +17 mm with 0.02 mm voxels. Various slices of the reconstructions can be seen in Figure 12 with different frequencies can be observed in Figure 13. With the ImageJ software built-in image profiling function, an intensity profile through the middle of each hair was used to estimate the full width at half maximum (FWHM) of each hair on each slice. Each hair diameter was estimated along 4 directions (X and +). A representative plot profile can be seen in Figure 15. For each slice also estimated the distance from each hair to the center of reconstruction (axis of rotation).

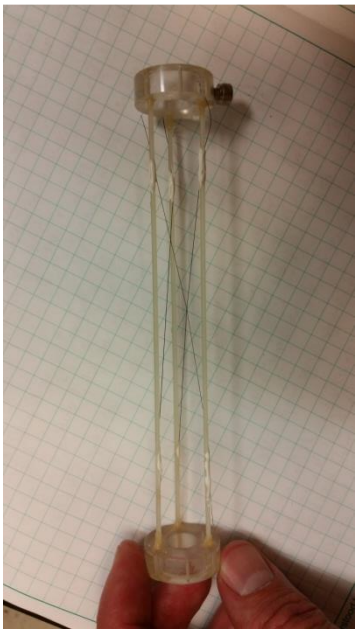

(a) Photograph of the hair phantom

(b) 3D OAT reconstruction of a hair phantom

Figure 12: Photograph of a hair phantom and the resultant 3D OAT reconstruction

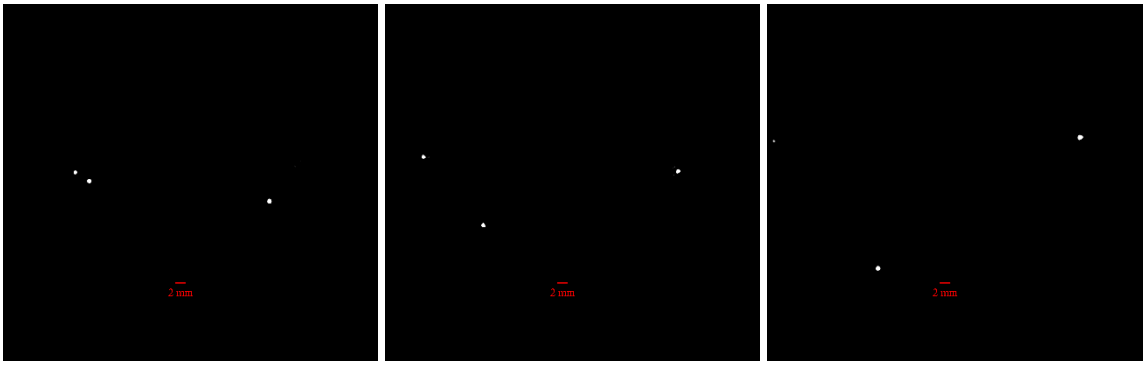

(a) (b) (c)

Figure 13: Three cross-sections through the reconstruction of the hair phantom acquired at 25 MHz and with 0.02 mm voxel size. The vertical position of the slice is (a) -10 mm, (b) 0 mm, and (c) +10 mm to the center of the array probe.

(a) (b) (c)

Figure 14: Central horizontal sections of the hair phantom at different sampling frequencies: (a) 20 MHz, (b) 25 MHz, and (c) 40 MHz

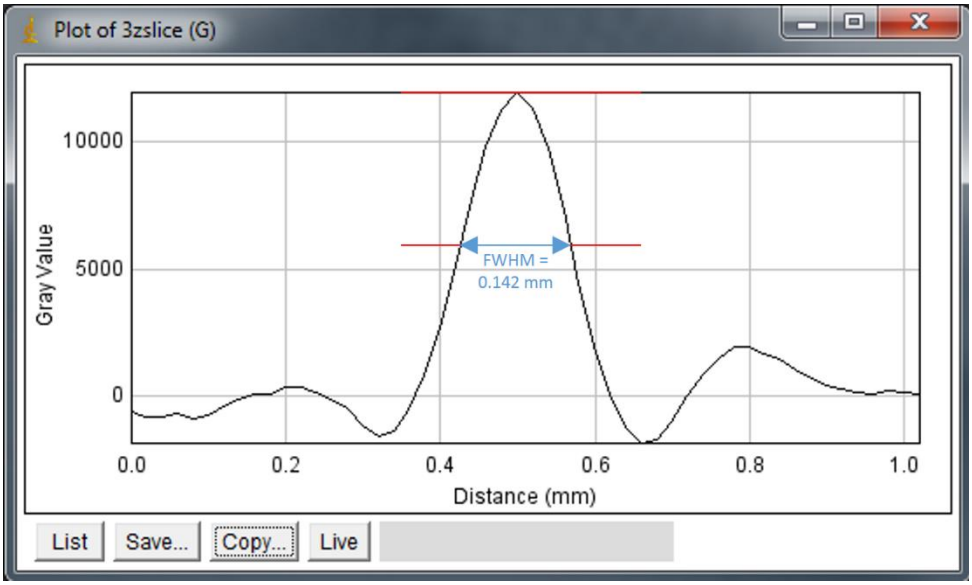

Figure 15: An example of the image intensity profile through one of the hairs at the central horizontal section.

The diameter of the hairs at the various slices of depths along the axis of rotation can be seen in Table 5. It was observed that the further away from the focus, the larger the diameter the hair was. Distance from the center was the estimated distance from the hair to the axis of rotation. The hairs were seen to be around 0.14 mm at the central slice but increased to be 0.28 mm at the furthest measured slice of -17 mm below the focus. The variations of hair the diameters on these furthest slices could be possibly due to more inconsistent illumination.

Table 5: Transverse image resolution at 25 MHz sampling rate. Z slice – position of the horizontal slice with respect to the equator, Dist. From Ctr. Distance from the axis of rotation, Average – FWHM of an image, Std. Dev. – standard deviation.

	Hair 1			Hair 2			Hair 3			All 3 Hairs	
Z slice	Dist. From Ctr.	Average	Std. Dev.	Dist. From Ctr.	Average	Std. Dev.	Dist. From Ctr.	Average	Std. Dev.	Average	Std. Dev.
-17	3.027	0.360	0.043	4.050	0.255	0.077	5.416	0.175	0.019	0.263	0.092
-10	3.788	0.165	0.010	4.748	0.170	0.012	5.425	0.165	0.010	0.167	0.010
0	4.7	0.145	0.010	7.155	0.140	0.016	5.013	0.140	0.016	0.142	0.013
10	6.314	0.180	0.016	5.476	0.165	0.010	8.866	0.200	0.016	0.182	0.020
17	6.847	0.310	0.038	6.407	0.310	0.012	9.902	0.240	0.059	0.287	0.051

Table 6 is of the central slice with three sampling frequencies of 20, 25 and 40 MHz. It can be seen in these results that resolution can be as sharp as 0.13 mm at 40 MHz to 0.15 mm at 20 MHz. However most scans were done with a 25 MHz sampling rate as with 1536 total samples and a speed of sound of ~1.52 mm/μs would provide an imaging depth of over 93 mm.

Table 6: Transverse image resolution (central horizontal slice) at different sampling rates

	Hair 1		Hair 2		Hair 3		All 3 Hairs	
	Average	Std. Dev.	Average	Std. Dev.	Average	Std. Dev.	Average	Std. Dev.
20 MHz	0.165	0.010	0.155	0.025	0.140	0.000	0.153	0.018
25 MHz	0.145	0.010	0.140	0.016	0.140	0.016	0.142	0.013
40 MHz	0.130	0.012	0.125	0.010	0.145	0.019	0.133	0.016

2-3-2: SENSITIVITY

A comprehensive series of tests involving solutions and contrast agents were done to determine the sensitivity of the system. The first was using solutions of cupric sulfate in

a phantom that consisted of six tubes of polytetrafluoroethylene (PTFE) with an inner diameter of 0.635 mm. Five of the tubes were decreasing by approximately one-half each time of cupric sulfate concentrations: 1, 0.5, 0.25, 0.125, 0.0625 OD as measured in an Evolution 201 spectrophotometer (Thermo Scientific, Waltham, MA). The sixth was a nickel sulfate solution of ~1 OD for reference.

After an eight average scan of 320 steps, the results of a thick 1 mm slice can be seen in Figure 16. Signal processing consisted of PCA for the first component on all the channels and on all the acquisitions, Wiener deconvolution of the inverted AE-IR. LOIS-View (a custom-designed visualization software based on Slicer3D) along with a TomoWave designed segmentation module which can do 2D or 3D segmentation by drawing on at least one (single slice), two (beginning and end of the volume), or more regions of interest. The TWL_Segmentation module would then interpolate the regions of interest and provide various statistics such as mean, median, etc.

Table 7 shows the estimated optical fluence and the statistics of each tube after creating a 0.6 mm diameter cylinder of 10 mm height around the central focal plane of the probe for each tube. A similar method was also used to measure the noise in the reconstructed volume in the same slices that were used to create the statistical ROI for each tube. The signal-to-noise ratio (SNR) was then calculated based on subtracting the tube mean by the noise mean and dividing the result by the standard deviation of the noise.

The SNR of the 0.27 cm^{-1} tube was seen to be over fourfold over the background. In addition, it was seen that it was possible to discern the concentrations that were even lower such as 0.06 OD (~0.14 cm^{-1}) as its SNR was 2.7. Only a single 750 nm wavelength was used to scan and a plot of the image brightness vs. μ_a can be seen in Figure 17. The R^2

of this linear trendline is above 0.99. Taking into consideration that laser fluence could still be increased more than four times, the found value of the minimal detectable optoacoustic image contrast is $\delta\mu_a$=0.03 cm^{-1}, which is about 3 times more sensitive than the highest molecular image contrast value reported in the literature [58]

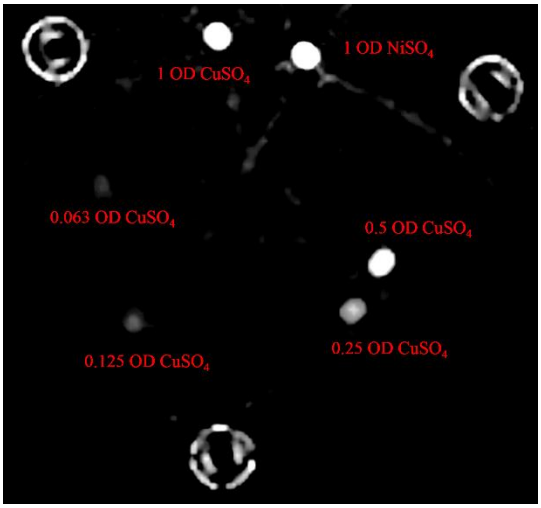

Figure 16: 1 mm thick slice through the phantom at 750 nm wavelength showing all tubes visible

Table 7: Statistics from the scan of a phantom that shows better even better sensitivity with more laser power as compared to the previous experiment

Laser Output	170mJ	at 750 nm			
Estimated optical fluence on tubes			~ 4.7 mJ/cm^2		
Object	$\mu_a(cm^{-1})$	Mean	Median	Std Dev	SNR
1 OD NiSO4	2.25	799.03	806.76	248.10	55.24
1 OD CuSO4	2.21	747.76	753.85	217.16	51.60
0.5 OD CuSO4	1.12	380.80	393.54	123.14	25.59
0.25 OD CuSO4	0.55	165.53	170.09	61.47	10.33
0.13 OD CuSO4	0.27	79.37	78.20	29.60	4.22
0.06 OD CuSO4	0.14	57.97	61.27	21.61	2.71
Noise Tube	NA	19.77	17.27	14.11	NA

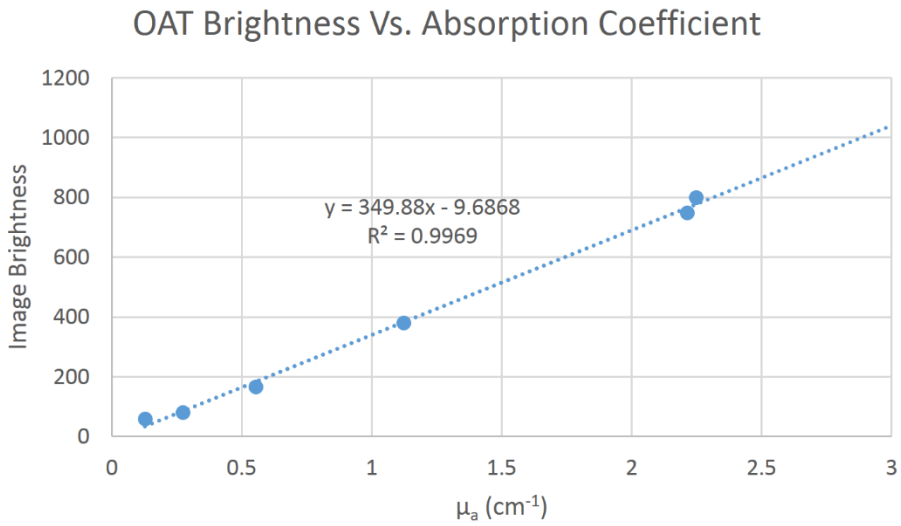

Figure 17: Linear regression plot of the image brightness versus absorption coefficient of the tubes at a single wavelength, 750 nm

Another set of sensitivity tests involved synthesized melanin-like nanoparticles (MNP). The protocol of conjugation and fabrication of MNP-PEG is further detailed in Dr. Liopo's article [33]. The phantom was a custom-made bracket that supported two flexible silicone tubes with an internal diameter of 510 µm and a wall thickness of 150 µm. One tube was filled with GNR nanoparticle suspension and the other was filled with MNP suspension in water. To separate GNR tube from MNP tube on optoacoustic images, the former had one knot and the latter had two knots. This phantom was used to perform a series of quantitative imaging experiments with LOIS-3D using pulsed laser energy at 800 nm with a total effective optical fluence of 2.5 mJ/cm^2 at the phantom. Imaging experiments were repeated three times with different concentrations. The average brightness of optoacoustic images was measured in the central area of the images illuminated more evenly than the adjacent areas. The measurement of brightness in the tubes was done using the system's segmentation software. Each tube was identified and

their mean brightness and standard deviations were calculated based on their image brightness values from the central area of the images, i.e. in the knot area of GNR tube and in the straight portion of the MNP tube between the knots. The reason for GNR being chosen as a comparison to MNP is due to their strong optical absorption resonance in the near-infrared and spectral tenability based on aspect ratio, GNRs have become the gold standard for optoacoustic contrast agents [59].

OAT experiments demonstrated the optoacoustic brightness of melanin nanoparticles relative to that of gold nanorods and measure the image brightness as a function of MNP concentration. OA image of a phantom containing two silicone tubes with an internal diameter of 510 μm was acquired. Figure 18a depicts an image of GNR tube having a single knot (left) and MNP tube with two knots (right), both having equal optical density OD=1.0. Optoacoustic contrast presented in Figure 18b presents an average image brightness M ± SD over the central area evenly illuminated by the about equal optical fluence (knot area of the GNR tube and vertical area of the MNP tube). The imaging experiment was repeated three times. The average pixel brightness was found (considering experimental errors) had MNP being a bit less than GNR (Figure 18b). Because the wall thickness was 150 μm we could estimate the image resolution ($d < 0.3$ mm) from the fact two tubes touching each other in the knot were well separated (see Figure 18a).

Further, the tubes were filled with two times and four times diluted concentrations of GNR and MNP. A linear correlation between the nanoparticle concentration and the optoacoustic image brightness was found (Figure 19).

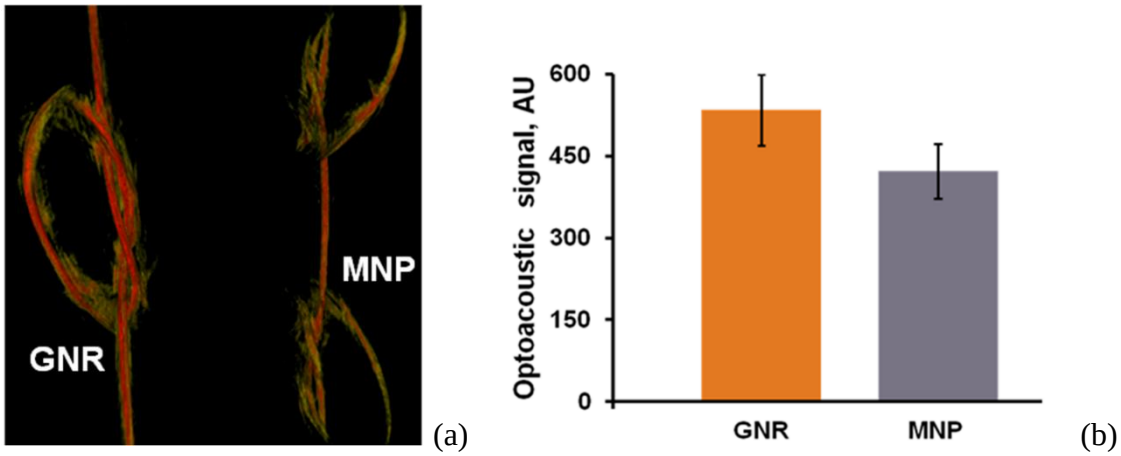

(a) (b)

Figure 18: (a) OA image of two silicone tubes with GNR tube having a single knot (left) and MNP having two knots (right), both had an equal optical density of 1.0. (b) The average optoacoustic brightness Mean ± SD of the tubes with GNR and MNP.

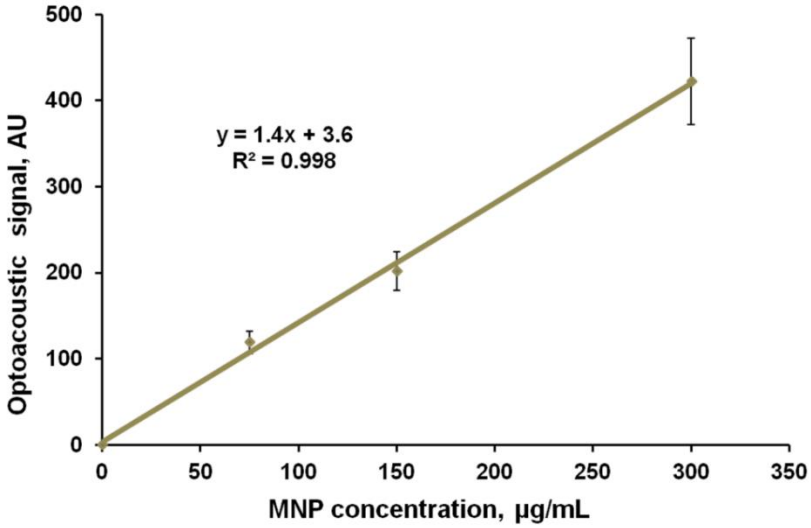

Figure 19: Optoacoustic image brightness of MNP, showing linear dependence as a function of concentration with points on the graph corresponding to the optical density of 0.25, 0.5, and 1.0.

The signal-to-noise measurements performed in this experiment permitted an estimate of the system sensitivity. The minimum optoacoustic brightness that could be detected above the noise corresponded to the optical density of OD=0.1, which corresponds to μ_a=0.23 cm^{-1} in the tube illuminated with a combined effective optical fluence of about 2.5 mJ/cm^2. Should one apply the maximum safe level of the optical fluence permitted by

ANSI (20 mJ/cm^2) the minimum detectable change in the optical absorption coefficient will become ~0.03/cm which coincides once more to previous sensitivity experiments.

A third experiment was done with ICG due to its availability as an FDA-approved contrast agent for human IV administration for fluorescence [60, 61]. A more complex scattering gelatin phantom in the shape of a cylinder with a height of 100 mm and a diameter of 25 mm was created using 5% agar, 1 part water, and 4 parts whole milk to achieve an effective scattering of about 7.5 cm^{-1}. Inside the cylinder, we embedded three PTFE tubing from Zeus of inner diameter 0.635 mm and wall thickness of 0.051 mm around 7 mm deep from the outer surface of the cylinder. Scans were done at two wavelengths (730 and 780 nm) with three different concentrations of ICG (0.007, 0.005, and 0.0025 mg/mL) where the corresponding absorptions can be seen in Figure 20a.

Laser fluence was measured to be an estimated 2.4 mJ/cm^2 on the phantom for 730 nm and 4.0 mJ/cm^2 for 780 nm. Segmented regions of each tube for the two wavelengths were analyzed and normalized between the two laser fluence with the means plotted into an image brightness versus absorption which is shown in Figure 20b. Using the same methodology of SNR as cupric sulfate, ICG seems to show a minimal absorption of 0.15 cm^{-1} or 516 pmol/mL at 780 nm. This could be further improved with more laser fluence closer to the safety limits to 0.03 cm^{-1} or 64.5 pmol/mL.

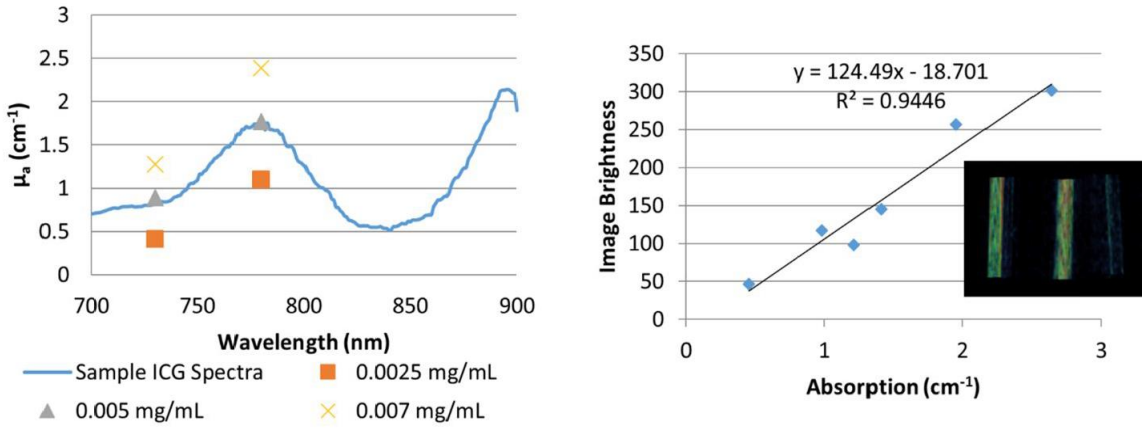

(a) (b)

Figure 20: ICG (a) spectra for the two scanned wavelengths and the (b) linear trendline from the image brightness versus absorption after taking into account laser fluence.

These experiments helped estimate the minimum optical absorption coefficients detectable with SNR=2 relative to the background image brightness. Assuming that the image contrast increases linearly with the incident optical fluence, we calculated the average optical absorption contrast that can be detected with our qOAT system utilizing the optical fluence of 20 mJ/cm^2, safe for laser illumination of skin [52]. The found value of the minimal detectable optoacoustic image contrast is $\delta\mu_a$=0.03 cm^{-1}, which is about 3 times more sensitive than the highest molecular image contrast value reported in the literature [58].

CHAPTER 3: APPLICATIONS IN ANATOMICAL IMAGING

Mice are often used as a mammalian model for human disease in preclinical research as the mouse and human genomes are 85% identical where some genes are 99% identical and others just 60%. This provides a path for a scientist to mimic certain effects of DNA alteration that occur in human diseases which in turn provides a model to test therapeutic agents and their effects [62]. Optoacoustics and specifically LOIS-3D with its high optical contrast and penetration provide a means to seen certain organs such as the kidneys and spleen as well as blood vessels within the mouse [39, 43].

3-1: Mouse Body

The LOIS-3D system as described in Chapter 2 was used to image the internal organs and blood vessels of the mouse. 755 and 1064 nm were chosen to be used as they would later also undergo functional image processing. Deoxy-hemoglobin was known to absorb more at 755 nm whereas the opposite was true with oxy-hemoglobin absorbing more at 1064 nm. The mouse was scan with 320 angular steps and 64 averages and the laser fluence recorded for reference with 757 nm having around 110 mJ and 1064 nm with 280 mJ. The scan was interleaved such that it would go 755 nm – 1064 nm – 755 nm – 1064 nm until all the required acquisitions for each wavelength were saved before moving onto the next angular position. This was to minimize the variance between the two scans due to movement artifacts as we minimized the time delay between different wavelength acquisitions to 100 ms which was the repetition rate of the laser.

Mice were kept in a degassed water bath with a temperature of 36°C with the help of a water circulation system and with the mouse asleep due to isoflurane anesthesia of

1.5% and a flow of ambient air to the mouse of 1.8 liters per minute which would provide air to the mouse while submerged. The mouse and the mouse can be seen inside the imaging module in Figure 21 with the red square in each image an estimate of the illumination area of the mouse. Care was given to ensure that air was always flowing to the mouse even while submerged in water as the camera could see as high as the water-air interface at the top of the imaging module to the focal region of the probe so that it can always be observed if the mouse was breathing and if needed, the air was flowing out of the cylinder head as proof of a diving bell effect.

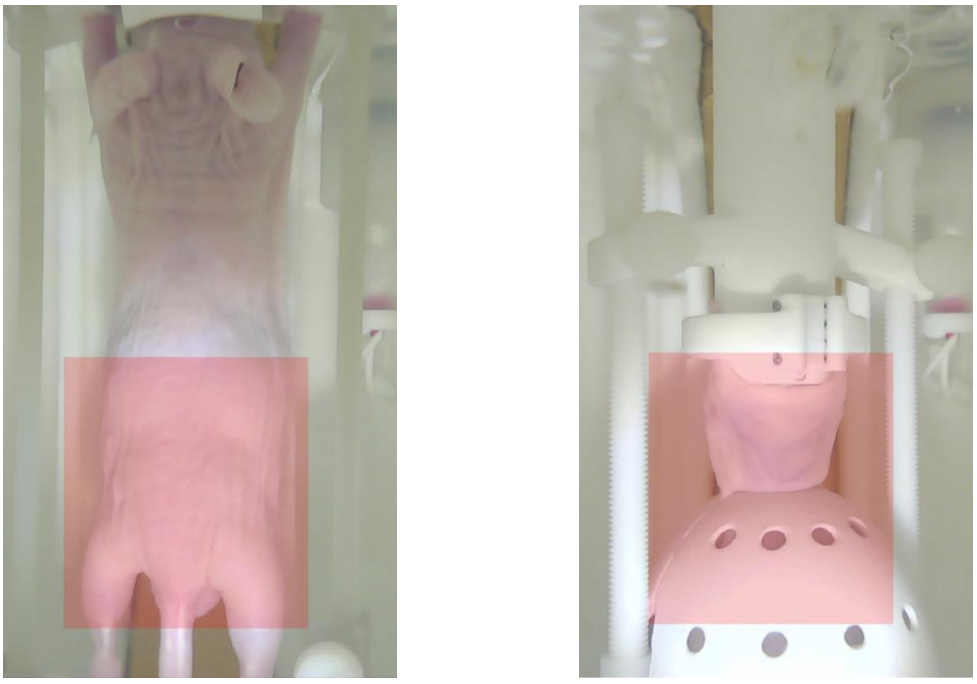

(a) (b)

Figure 21: Mouse scan with the (a) body being scan and (b) brain being scanned

Figure 22 shows the optoacoustic volume of a mouse lower body at 755 nm and Figure 23 corresponds to 1064 nm. The results from the mouse scan show that at both wavelengths the caecum, spleen, left and right kidneys, vertebrae, liver, and intestines are seen. In addition, there are several blood vessels seen at both but certain ones such as the peripheral blood vessels are seen in greater sharpness at 755 nm.

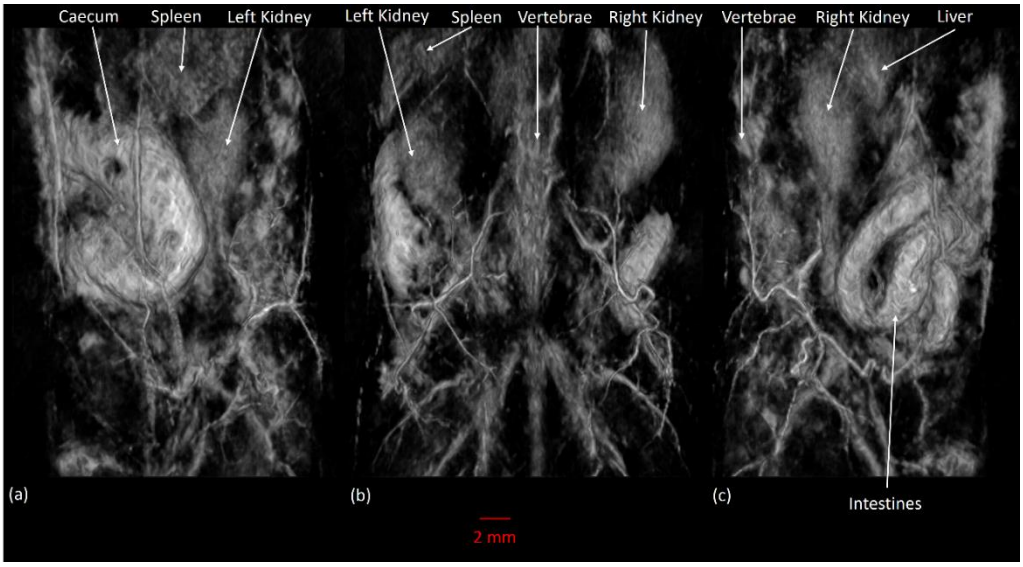

Figure 22: Mouse body scans at 755 nm wavelength with different orientations of the mouse: (a) left side, (b) backside, and (c) right side

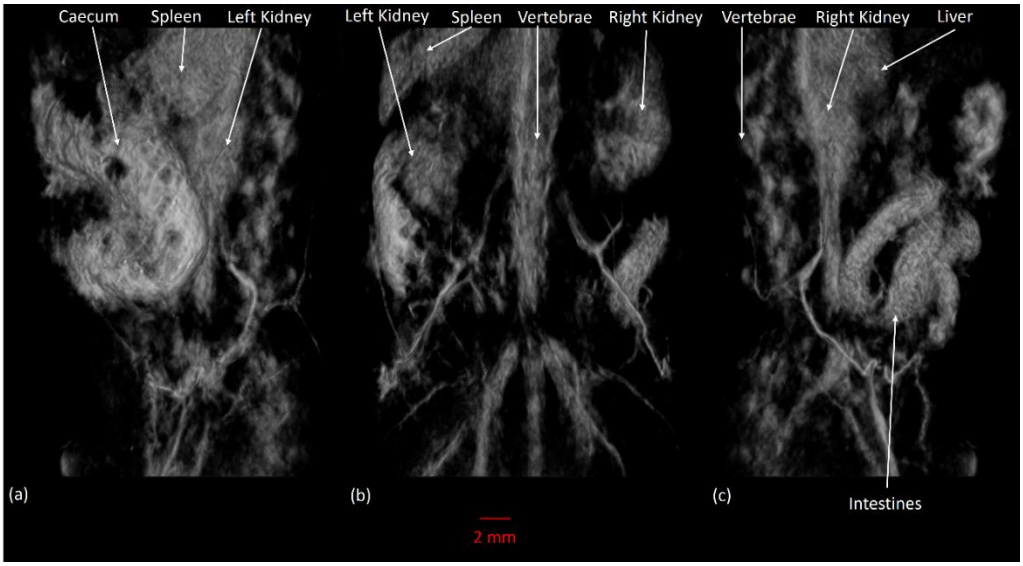

Figure 23: Mouse body scans at 1064 nm wavelength with different orientations of the mouse: (a) left side, (b) backside, and (c) right side

It was seen here and investigated further in the next chapter that these differences seen between 755 and 1064 nm wavelengths would help differentiate highly oxygenated from low oxygenated once more processes were accounted for.

3-2: Mouse Brain

Figure 24a shows the 755 nm OAT and 24b shows the 1064 nm OAT image from the crown of the head to compare to the corresponding atlas slice of 24c as seen in Iwaki's book [63]. There are identifiable features seen such as the dorsal sagittal sinus and the transverse sinus. Features of the blood vessels that provide the cerebellum shape can also be seen. Overall the major features are seen at both wavelengths with certain smaller blood vessels being seen more at 755 nm as compared to 1064 nm.

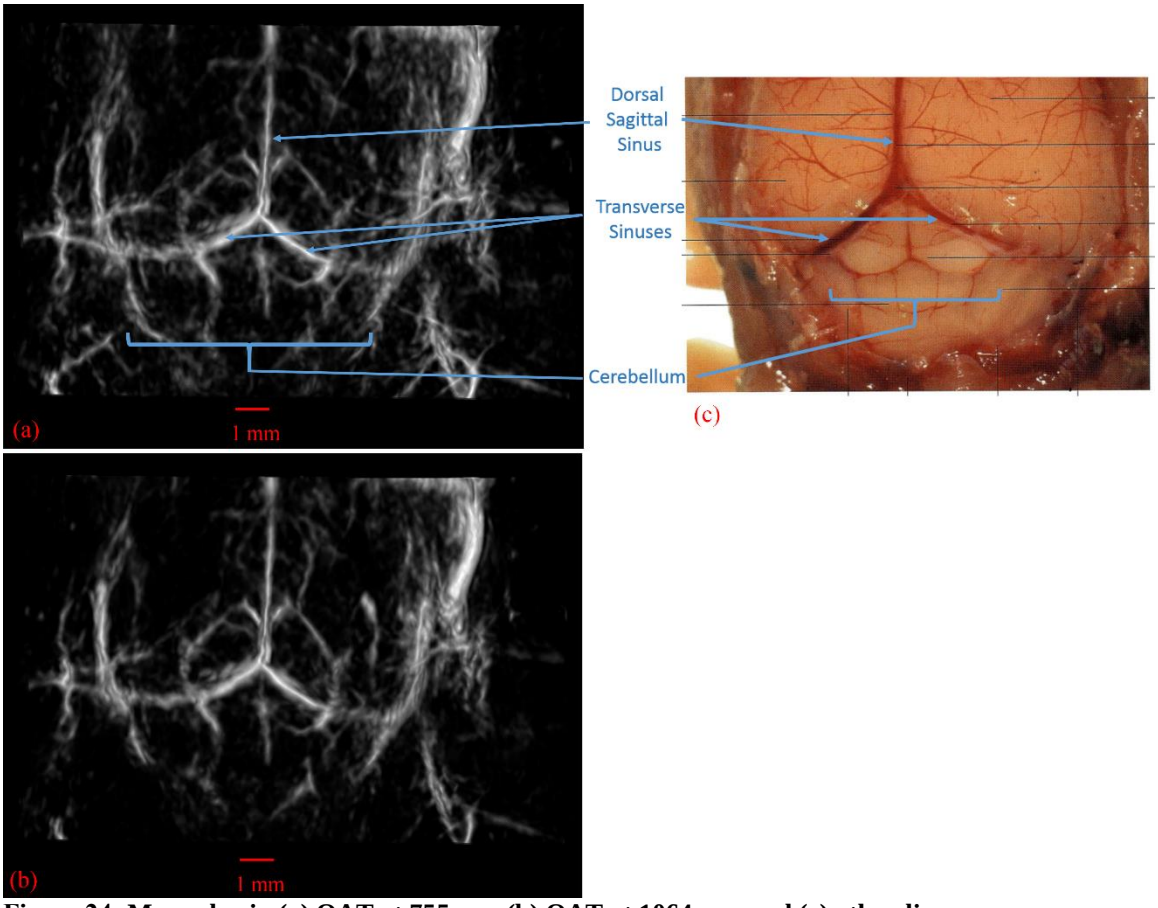

Figure 24: Mouse brain (a) OAT at 755 nm, (b) OAT at 1064 nm, and (c) atlas slice

CHAPTER 4: APPLICATIONS IN MOLECULAR IMAGING

Contrast agents are commonly used in medical imaging as a means to introduce contrast in an area which there would not have been otherwise. With the high sensitivity of the system proven in phantoms, the LOIS-3D system was proposed as a non-invasive system that can observe long-term biodistribution of contrast agents and be able to detect the presence of targeted contrast agents in areas of interest.

The first application for biodistribution was with gold nanorods (GNR) which have a strong tunable plasmon resonance in the near-infrared range and can be covered in polyethylene glycol (PEG) to become more biocompatible within the body. The LOIS-3D system would do scans of the whole mouse to track the GNR distribution throughout the mouse body, accumulation over time in certain organs, and even see the eventual decrease of GNR concentration in those very organs. The second study was done with a targeted fluorescent contrast agent IRdye800-Tilmanocept as they are already widely used in the present medical field. The question was to determine the efficacy of the LOIS-3D system to see the deposits of the Tilmanocept around the tumor of a mouse and provide estimates in the concentration of contrast agents that were deposited.

4-1: Biodistribution of Gold Nanorods

Gold nanorod fabrication and stabilization were investigated by Dr. Liopo and details into the production of the GNR were published by Su and Liopo [39, 64]. The laser operated with an output laser energy of ~70 mJ/pulse for 765 nm and ~200 mJ/pulse for 1064 nm.

Mice studies consisted of four athymic nude-foxn1^{nu} mice (Harlan, Indianapolis, Indiana), 7-9 weeks old were studied. Animal handling and isoflurane anesthesia were done in the same manner in chapter 3-1-1. The mice would be injected with 400 μl of the GNR solution (19 mg of Au per kg of body mass) intravenously (IV) through the tail vein. Each mouse was scanned with 765 and 1064 nm wavelength at intervals of pre-injection, 1, 24, 48, and 192 hours to investigate the biodistribution of untargeted GNR. The GNR that was used had a maximum plasmon resonance around 760 nm and had very little absorption at 1064 nm so 1064 nm was thought to have been a control scan. The spectra of the GNR-PEG can be seen in Figure 25.

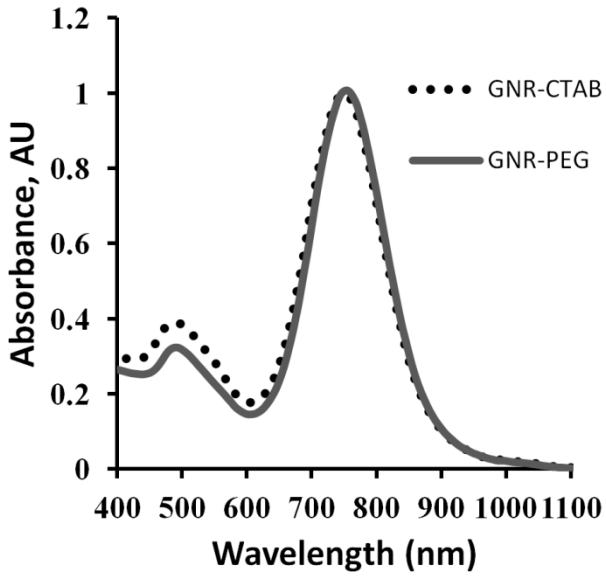

Figure 25: Spectra of the GNR pre-PEGylation and post-PEGylation showing minimal changes to the absorbance spectra

Three orthogonal projections (dorsoventral (a), left mediolateral (b), and right mediolateral (c) views) of the OA volumes reconstructed from a mouse before GNR injection as well as 1, 24, 48, and 192 hrs after the injection of GNRs are shown on Figures

26 and 27. The areas of the image that were used for the analysis of organ-specific changes in the image brightness are outlined. These regions of interest were the spine, kidneys, spleen, and whole body. Analysis of organ-specific changes of the optoacoustic contrast used two-dimensional grayscale projections of the three-dimensional reconstructed volumes. The left mediolateral view of a mouse was used for manual segmentation of the spine, left kidney, spleen, and the whole body. The right mediolateral view of a mouse was used for segmentation of the spine, right kidney, and the whole body. Dorsoventral view of a mouse was used for segmentation of kidneys, spleen, spine, and the whole body. The average brightness of the segmented regions was evaluated and the brightness enhancement coefficient (*BEC*) was calculated as

$$BEC = \frac{B_{ROI}[t] - B_{ROI}[t_0]}{B_{ROI}[t_0]} \times 100 \qquad (7)$$

where $B_{ROI}[t]$ is the average brightness in the region of interest (ROI), like the spleen or the whole body, measured at time moment t following the injection time t_0.

Enhancement of the 765 nm image intensity, particularly in the areas of the spleen and spine, is seen after the injection of GNRs (Figure 26). The overall image background is also significantly higher than that of the control imaging, reaching the maximum in 1 day following the GNR injection. Figure 26 displays average brightness in the regions outlined on the OA images that were reconstructed from the control scans (before the injection of GNRs). Only data obtained from the same scan (765 nm or 1064 nm) can be compared, due to different incident fluences and light distributions within the tissue for the two laser wavelengths. The kidneys are visualized as the brightest organs on the

optoacoustic images due to both high vascularization and water content. The spine is vaguely seen at 1064 nm. However, it is quite bright at 765 nm.

Similar to 765 nm, but more dramatic, enhancement of the image brightness is observed after the injection of GNRs on 1064 nm optoacoustic images (Figure 27). However, the areas (organs) of interest on the control image (before injection of the GNRs) at 1064 nm have the contrast much smaller than those at 765 nm. The overall image background also increases in comparison to the control imaging, reaching the maximum in 2 days following the GNR injection.

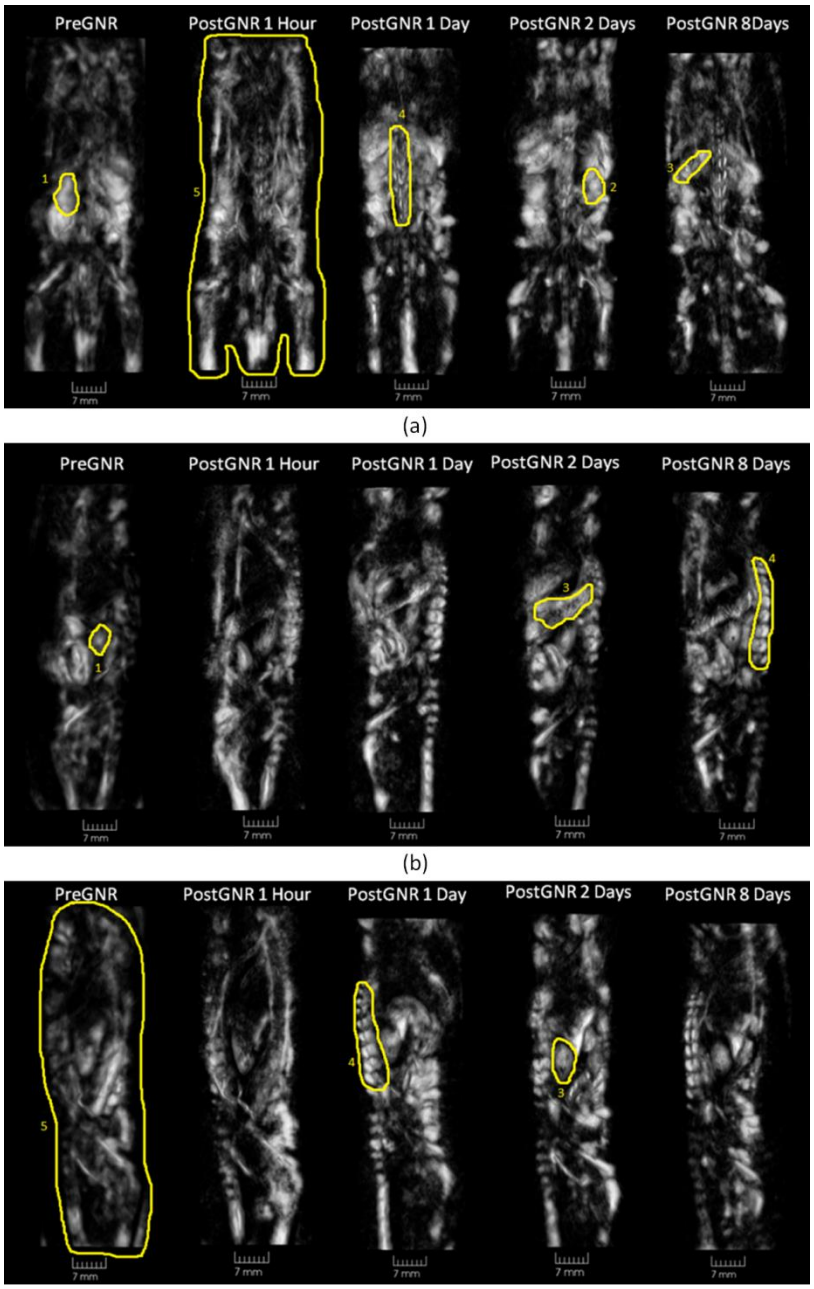

Figure 26: 765 nm scan of one of the mice over the span of 8 days post-GNR injection

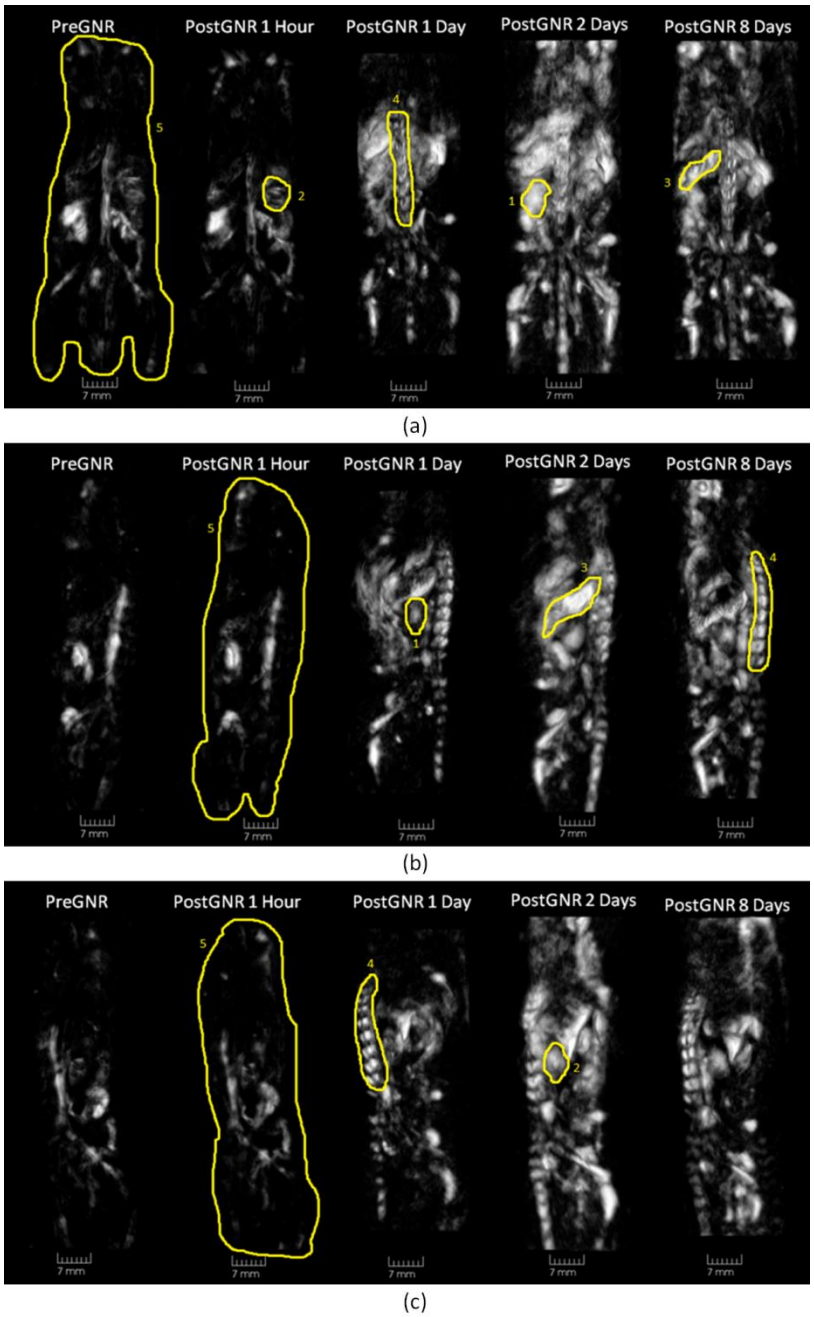

Figure 27: 1064 nm scan of one of the mice over the span of 8 days post-GNR injection

Figure 28 shows the changes of *BEC* inside the selected regions following the injection of GNRs. Similar trends are observed for all the organs as well as the whole body. The maximum brightness achieved 24 hours and 48 hours after the injection of GNRs on images acquired with 765 nm and 1064 nm illumination, respectively. The quick increase

in the image brightness is followed by a much slower decline, which may be indicative of slow excretion rates for the gold nanorods. Also, one hour after an injection of the contrast agent, there are noticeable increases in the brightness on 765 nm images of the spleen, spine, and the whole body. At the same time, no changes in the brightness are visible on 1064 nm images. 24 hours after the injection of GNRs, brightness on 1064 nm images increases dramatically.

Figure 29 shows the light absorption spectra of GNR samples incubated with blood for 1 hr and 24 hrs. PEG-GNRs demonstrated stable optical properties while incubated for 1 hr with blood. However, after a long time of incubation with blood a characteristic plasmon resonance peak of PEG-GNRs decreased, broadened, and shifted towards the infrared region due to aggregation [65].

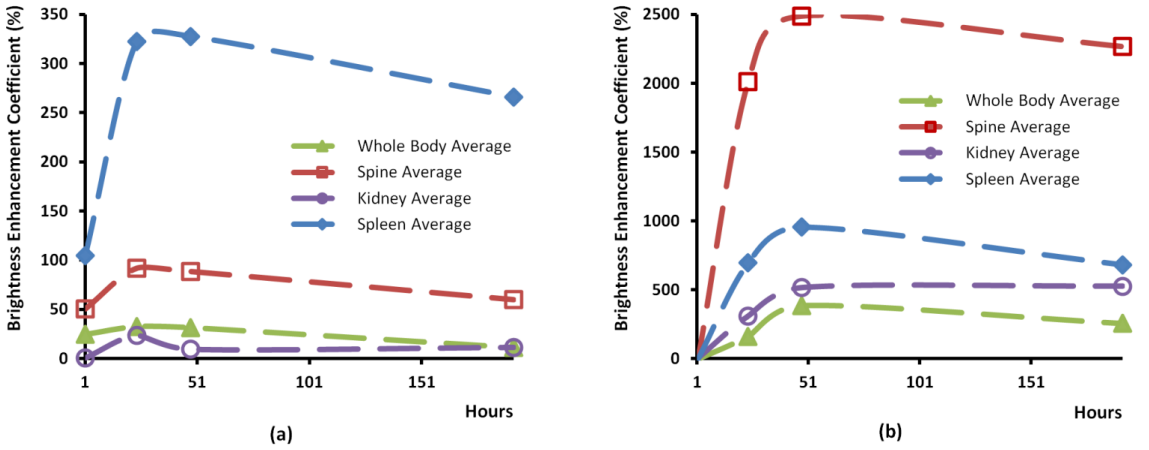

Figure 28: Trend of image brightness over time for the four regions of interest at (a) 755nm and (b) 1064nm

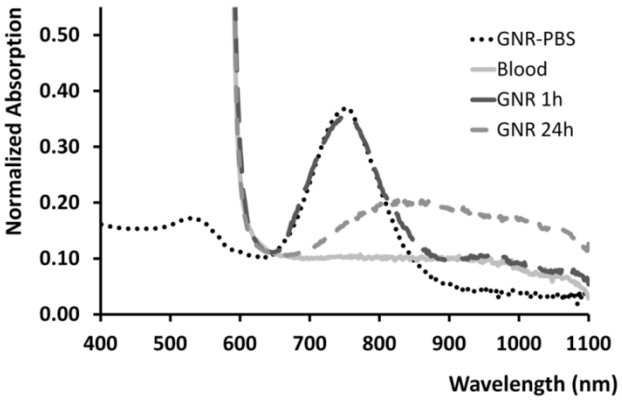

Figure 29: Samples of GNR intubated in blood outside of the mouse which can be seen to gradually broaden its absorption spectra over time

It was observed in other publications that PEG-coated nanoparticles are redirected to the reticuloendothelial system to the mononuclear phagocyte system [66, 67]. Maltzahn et al [68] showed that a single intravenous injection of PEG-GNRs resulted in a long circulation time of up to $t_{1/2}$=17 h. In that study, the total dose was 20 mg of gold per kg of body mass and did not induce any toxicity in mice. Our findings were in agreement with that data showing that 20 mg of GNRs per kg of body mass did not produce any pathological changes in mice. Therefore, we exclude the chance that any short-term (up to 24 hrs) changes observed on OA images could be caused by toxic effects of GNRs.

Enhancement of brightness on 765 nm optoacoustic images were interpreted as a local accumulation of GNRs. Maximum levels of brightness were observed 24 hours post-injection, followed by a slow clearance trend for the next 6-7 days. The observed enhancement of optoacoustic contrast is consistent with previously observed biodistribution of GNRs into different tissues, organs, and cells [69-71]. Tong L. et al [66] described PEG-GNRs as having well-established ‘‘stealth’’ properties that can shield nanoparticles from fouling by serum proteins and can reduce their rate of clearance by the

reticular-endothelium system. It was shown that the interaction of gold nanoparticles with various plasma proteins could affect their biocompatibility and therapeutic efficacy. An important fact was described by Niidome et al. comparing the biodistribution of CTAB-GNRs and PEG-GNRs in mice [72]. They reported that 30% of the Au from CTAB-GNRs was found in the liver 0.5 h after intravenous injection. In contrast, PEG-GNRs remained in the blood for a much longer period, with 35% of the Au accumulated in the liver after 72 hours.

Functional changes and the development of the post-injection optoacoustic contrasting were mapped using time-dependent optoacoustic imaging (Figures 28a and 28b). The PEG-GNR solution provided high optoacoustic contrast for a prolonged time of 8 days, significantly exceeding that currently achieved with standard imaging agents [69, 70]. Sections of the liver can be seen within Figures 26 and 27, above the right kidney in the 1, 2, and 8 days post-injection scans. This correlates to a study by Lankveld et al [73], as large concentrations of GNRs were observed in the liver 1–6 days following their intravenous injection. This also conforms to the silver staining and Hematoxylin stain where increases in GNR were found in the liver even after 3 days but was seen to have decreased in concentration on day 8.

In conclusion, we presented a study showing that the LOIS-3D optoacoustic system is adept to detect long-term changes in the distribution of the injected contrast agent *in vivo* which the trends correlated to published articles as well as laboratory tests that were done by Dr. Liopo. It would be scientifically valuable to perform similar experiments to study the biodistribution of other OA contrast agents, such as carbon nanotubes and microbubbles. The potential physiological changes in vascularization, water content, and

blood oxygenation associated with the biodistribution of gold nanorods could be monitored using the proposed three-dimensional OA imaging method.

4-2: Tracking of Targeted IRDye-800 Tilmanocept

The last test was to confirm the ability of the LOIS-3D system to track the targeted IRDye-800 Tilmanocept contrast agent onto the tumor and provide estimates of the concentration of IRDye800 deposited on the tumor. The IRDye-800 Tilmanocept was prepared by the lab of Dr. Anne Wallace, MD, and David Vera, Ph.D. from the University of California, San Diego. The goal of this contrast agent was to identify cancerous lymph nodes and act as a better biomarker than the current dyes in use today [74]. Breast cancer xenograft was prepared in an orthotopic mouse model by the group at UCSD. The scan was done at 800 nm (~2.5 mJ/cm^2 on the skin) at pre- and 45 minutes post-injection of 100 mL of Tilmanocept+IRDye800 with a concentration of 2 mM/L or ~4 pmole.

Figures 30 and 31 show two mice before and after IRDye 800CW-Tilmanocept injection. The whole tumor was measured and the means can be seen in Table 8. The numbers in Table 8 are low in general due to the growth of the tumor being so large and in all likelihood, much of the tumor was dead cells due to necrosis and therefore did not have much blood especially inside the tumor. Still, even under this circumstance, it was seen to have around a 10% increase in contrast at the tumor post-injection.

IRDye 800CW-Tilmanocept has maximal optical absorption when loaded with 2.3 moles of IRDye800 per mole of Tilmanocept with a molar absorptivity (ε) of ~230 $cm^{-1}mM^{-1}$ [75], hence a 1 micromolar (uM) concentration would add the required optical absorption of $\Delta\mu_a$ ~0.23 cm^{-1} for optoacoustic imaging with a laser pulse of 2.5 mJ/cm^2. Strictly, IRDye800CW is a fluorophore and some of the absorbed energy is converted to

fluorescence photons (QY ~5%) leaving ~95% for optoacoustic imaging contrast and slightly increasing the detectability requirement to ~1.05 uM IRdye800CW-Tilmanocept. In vivo, we have demonstrated ~1.1 picomoles of IRdye800CW-Tilmanocept accumulating in a small tissue volume of ~1mm^3 (1 µL) [75] which provides an optoacoustic imaging detectable concentration of 1.1 uM (>1.05 uM). Even lower concentrations of IRDye 800CW-Tilmanocept would be detectable by increasing the pulse energy towards the ANSI limit if required.

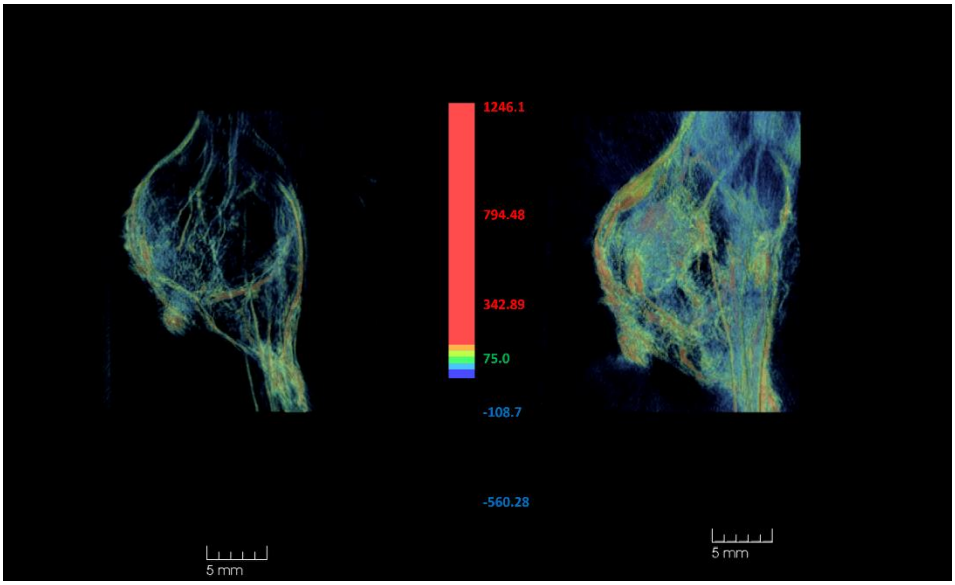

(a) **(b)**

Figure 30: Mouse 1 (a) Pre- injection and (b) Post- injection

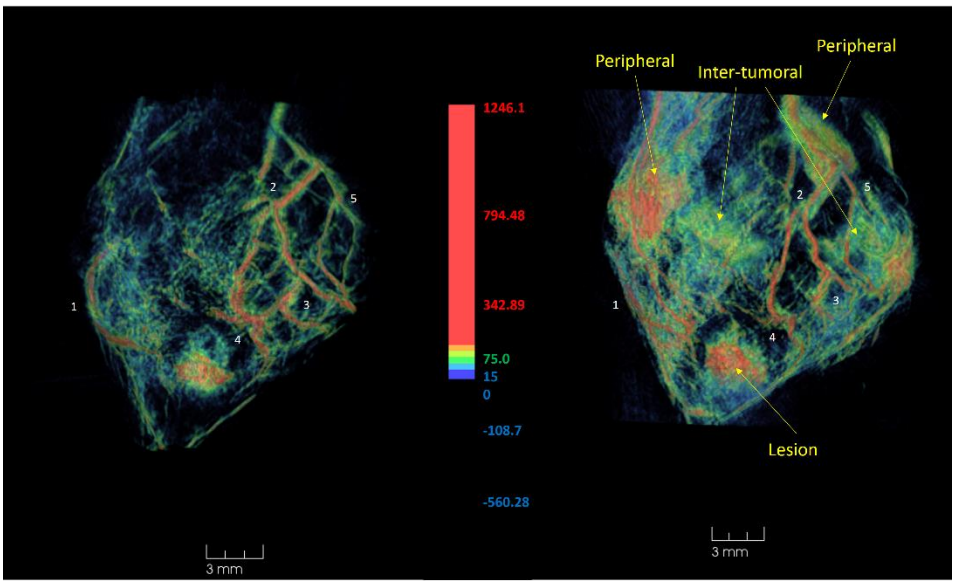

(a) (b)

Figure 31: Mouse 2 (a) Pre- injection and (b) Post- injection

Table 8: Increase brightness in both mice post-IRdye800 injection

	Mouse 1	Mouse 2
Pre-	87.3	56.9
Post-	95	63.4
% Diff	8.8	11.5

An investigation of the precision in optoacoustic tomography by Joseph [58] used the commercially available iThera Medical inVision256-TF (München, Germany). The probe was an incomplete ring of 270° angular coverage and 4 cm radius curvature and 256 focused transducers with a center frequency of 5 MHz. Their phantom mimicked the generic tissue as defined by Jacques [76] with the target solutions being contained in a thin-walled plastic straw of 3 mm diameter. ICG and IRDye800CW were two of the contrast agents investigated which can be compared. Detection limits were reported to be 100 nM for both contrast agents which were optical densities of 0.10 (IR800, 777 nm) and 0.084 (ICG, 778nm). The laser was estimated to have a fluence of somewhere in the range of 17

- 18 mJ/cm^2 depending on wavelength. In comparison LOIS-3D, was estimated to be ~2.5 mJ/cm^2 which is seven times less laser fluence so the estimated $\Delta\mu_a$ would go down from ~0.23 cm^{-1} to ~0.03 cm^{-1} had the laser fluence been equal between the two systems. Had the same laser fluence been used with the LOIS-3D system, then it would have had a sensitivity that would be three times better than the iThera Medical inVision256-TF [58].

4-3: Conclusion

The LOIS-3D system showed promising results in terms of being able to see different parts of the mouse. The ability to see a large portion of the mouse in one scan or to be able to image the brain is very promising. Considering the contrast seen at both wavelengths, one avenue to pursue is functional imaging and differentiating organs and blood vessels into blood oxygenation values.

Biodistribution was seen through a week-long study that gold nanorods would deposit in the kidneys and liver in a day or two with a downward trend seen after a week. Various publications show similar results and were also seen through our parallel laboratory studies. Another study into the fluorescent IRDye800 Tilmanocept, showed the capability of the system to track the targeted contrast agent at the tumor showing increased contrast of 10%. In addition, the ability of the system was seen to be able to detect picomoles of IRdye800CW-Tilmanocept accumulating in a small tissue volume of ~1mm^3 (1 µL) [75] which corresponded to a detectable concentration of 1.1 uM (>1.05 uM).

CHAPTER 5: TOWARDS FUNCTIONAL IMAGING

While optoacoustic has been proven to image living biological tissues for over a decade [1, 2], there is still the need for continuous advancements in functional imaging. While much of the work deals with multi-spectral de-mixing [77, 78] there is less of an emphasis on the variation in-depth penetration of each wavelength. That is more apparent when wavelengths are so far away from each other such as 755 nm versus 1064 nm where water absorption and variations of blood in tissues as reported by Roggan [79].

The supply of blood carrying oxygen and nutrients to tissues is important for the normal functioning of the tissues. Any deviation from normal blood supply causes immediate health problems: hypoxia, anemia, hypoglycemia (due to decreased blood concentration), or hematoma (due to increased blood concentration in the interstitial space). That is why imaging of vasculature, blood circulation, and blood distribution in tissues and measurements of [Hb] and [HbO2] concentrations is included. Important biomedical applications of functional imaging are in angiography (studies of blood hemodynamics in the body) and angiogenesis (studies of the microvascular network of aggressively growing cancerous tumors).

The hemoglobin in blood has near-infrared spectrum and absorption that changes in relation to oxygen saturation so a spectral analysis of deoxy-hemoglobin (Hb) and oxy-hemoglobin (HbO_2) is possible with the use of multi-wavelength studies [79, 80]. The optoacoustic pressure would then be defined as

$$P = k \times \mu_a(\lambda_1) \times F(\lambda_1) \tag{8}$$

$$= k \times \left[\varepsilon_{Hb}(\lambda_1) \times C_{Hb} + \varepsilon_{HbO_2}(\lambda_1) \times C_{HbO_2}\right] \times F(\lambda_1) \tag{9}$$

where k is the system constant (Grüneisen) that remains the same in a given system, μ_a is the blood absorption coefficient at wavelength λ_1, and F is the optical fluence at wavelength λ_1. ε_{Hb} and ε_{HbO_2} are the molar extinction coefficients for deoxy-hemoglobin and oxy-hemoglobin respectively with C_{Hb} and C_{HbO_2} are the concentrations of deoxy-hemoglobin and oxy-hemoglobin respectively.

When the spatial distribution of the optical fluence, $F(\vec{r})$ is known, and Gruneisen parameter, $\Gamma(\vec{r})$ of the thermoacoustic efficiency may be considered constant through the object of interest, one can obtain the spatial distribution of the optical absorption coefficient, $\mu_a(\vec{r})$ from the optoacoustic images. A study was done where it was demonstrated that the Grüneisen coefficient is dominated by hemoglobin as the main chromophore in the NIR 1 region and is therefore constant and can be removed during multi-wavelength studies [81]. Since the optical absorption spectra for the molecular extinction coefficients of oxygenated hemoglobin, $\varepsilon_{HbO2}^{\lambda}$, and deoxygenated hemoglobin, $\varepsilon_{Hb}^{\lambda}$ are well known [79], one can potentially determine concentrations of these molecules [HbO2] and [Hb] in the body. For purposes of functional biomedical diagnostics, parameters of the total hemoglobin, THb, and blood oxygen saturation, SO2 can be determined from optoacoustic images acquired at multiple wavelengths, λ_i of the optical illumination. In the simplest case when other tissue chromophores do not make a noticeable contribution to the overall optical absorption, the functional parameters THb and SO2 can be measured from optoacoustic images acquired at two wavelengths, λ_1, λ_2 as follows [1]

$$THb(\vec{r}) = [Hb](\vec{r}) + [HbO2](\vec{r}) = \frac{\mu_a^{\lambda_1}\left(\varepsilon_{HbO_2}^{\lambda_2} - \varepsilon_{Hb}^{\lambda_2}\right) - \mu_a^{\lambda_2}(\varepsilon_{HbO_2}^{\lambda_1} - \varepsilon_{Hb}^{\lambda_1})}{\varepsilon_{Hb}^{\lambda_1}\varepsilon_{HbO_2}^{\lambda_2} - \varepsilon_{Hb}^{\lambda_2}\varepsilon_{HbO_2}^{\lambda_1}} \text{ and} \quad (10)$$

$$SO2(\vec{r}) = [HbO2]/([Hb](\vec{r}) + [HbO2](\vec{r})) = \frac{\mu_a^{\lambda_2}\varepsilon_{Hb}^{\lambda_1} - \mu_a^{\lambda_1}\varepsilon_{Hb}^{\lambda_2}}{\mu_a^{\lambda_1}\left(\varepsilon_{HbO2}^{\lambda_2} - \varepsilon_{Hb}^{\lambda_2}\right) - \mu_a^{\lambda_2}(\varepsilon_{HbO2}^{\lambda_1} - \varepsilon_{Hb}^{\lambda_1})}. \quad (11)$$

It should be noted though that optical attenuation through tissue is a complex matter the deeper one goes so fluence at an object of interest can be a challenging matter to quantify in and of itself. There are ongoing attempts to sO_2 estimates in deeper tissue through more accurate fluence estimations through Monte Carlo simulations, iterative reconstructions, or analyzing spectral properties [82].

The goal is to obtain the optical absorption coefficient, $\mu_a(\vec{r})$ from the reconstructed absorbed energy density by removing the variations of optical fluence. For this to happen, we had to better co-register the images using a wavelength cycling laser, equalize the incident of laser fluence on the skin surface, normalize the laser fluence in-depth, calibrate the difference in laser fluence between two wavelengths. We would then analyze the fully normalized wavelength images to distinguish blood oxygenation.

5-1: Multi-spectral segmentation and co-registration

The major attempt of co-registration was to enable rapid switching of the laser wavelength with each next laser pulse to achieve wavelength-cycling illumination mode for the acquisition of co-registered images at two and three wavelengths. The basic functional optoacoustic imaging is based on two co-registered images, acquired at two laser wavelengths, one of which is predominantly absorbed by hemoglobin and the other by oxy-hemoglobin of blood. For the two images to be accurately co-registered, the optoacoustic signals need to be acquired at two different wavelengths within the time interval shorter than the time of live tissue motion to the distance equal to the size of the image voxel (0.1 mm). Cycling of the two illumination wavelengths within 100 ms provided a minimally

acceptable rate for functional imaging with a sufficient resolution of about 0.5 mm. This laser is also able to output cycles of multiple wavelengths sequentially (such as $\lambda 1 > \lambda 2 > \lambda 3 > \lambda 4$) to acquire spectroscopic data from a specific volume of live tissue. Figure 32 shows the interleave scans done at 755 and 1064 nm where a square is drawn in the same location where there is believed to be an artery. Within this 1 by 1 mm square, they have the same coordinates in both wavelengths where the same blood vessel is located and therefore show interleaving wavelengths having a positive effect in co-registration.

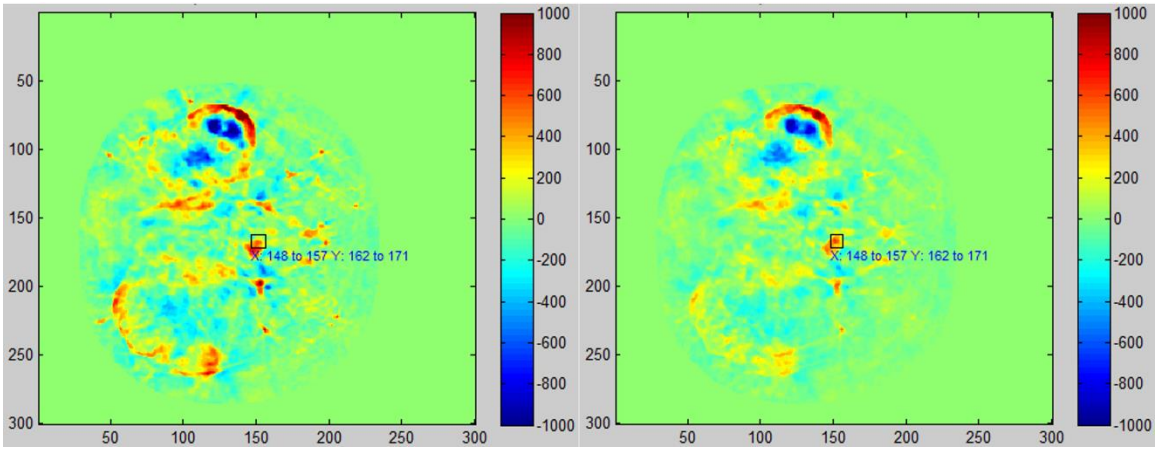

(a) (b)

Figure 32: The aorta can be seen within the black square with the same coordinates at both (a) 755 nm and (b) 1064 nm. A multiplier was applied to the 1064 nm wavelength based on Roggan's expected ratio for 100% sO_2 at 755 and 1064 nm wavelengths.

5-2: Fluence Normalization: Incident light on the skin, optical attenuation in-depth and between wavelengths

The method assumes that optical properties of arteries are known at all wavelengths in the NIR range [79] since arteries have 100% blood oxygen saturation. Arteries are the brightest objects at the wavelength of 1064 nm, and they are evenly distributed through the volume of live tissues. Veins are the brightest objects at the wavelength of 755 nm. The optical absorption of veins can be found based on known optical absorption coefficients of

oxy-hemoglobin and deoxy-hemoglobin and by comparing the brightness of the vein to the neighboring artery. Simultaneously, knowing the brightness of a vein and a neighboring artery of an optoacoustic image, it is possible to determine the blood oxygen saturation of the vein.

Conversion of the optoacoustic image of the absorbed optical density into a quantitative image of the optical absorption coefficient consists of three steps: (1) equalization of the incident optical fluence on the skin, (2) normalization of the optical fluence through the volume of live tissue, (3) calibration of the voxel brightness between two wavelengths used for functional imaging.

In the first step, the brightness of all voxels that belong to the blood vessels in the skin (arteries at 1064 nm and veins at 755 nm) are made equal by extracting the maximum brightness along the skin which are attributable to the blood vessels. A polynomial curve fit is applied to create a uniform illumination across the surface of the skin.

The second step is to normalize the voxel brightness through the depth of tissue volume. We create one voxel thick layer of tissue under the skin and take a voxel step into the depth of tissue along the radius pointing towards the axis of rotation. Maximum voxel brightness in each tissue layer that belongs to an artery at 1064 nm and vein at 755 nm is measured, recorded, and plotted as a function of depth. The maximum voxel brightness selected in each layer tissue along the depth axis can be used to estimate the exponential trend of the optical fluence attenuation as a function of depth.

Figure 33 depicts curves of maximum voxel brightness as a function of depth in a mouse body measured from the experimental data of 3D optoacoustic images of a mouse acquired at two wavelengths, 755 nm (Figure 33a) and 1064 nm (Figure 33b). These curves

show the heterogeneous distribution of blood vessels of various sizes. Highly vascularized tissue also can contribute to maximum voxel brightness. Nevertheless, these curves can reveal the averaged exponential attenuation trend of optical fluence attenuation as a function of depth.

Visualization of the two images can be found in Figures 22 and 23 before any sort of normalization. Red curves in Figure 33 (a, b) represent exponential extrapolations of the experimental curves according to Lambert-Beer's law. An average effective optical attenuation coefficient, μ_{eff}, of the live mouse tissues has been determined at the wavelengths of 1064 and 755 nm used for the acquisition of optoacoustic images.

Finally, the brightness of all voxels in the tissue volume of interest was normalized at each of the two wavelengths using the effective optical attenuation curves along the radial direction from the skin layer into the depth of the live mouse body.

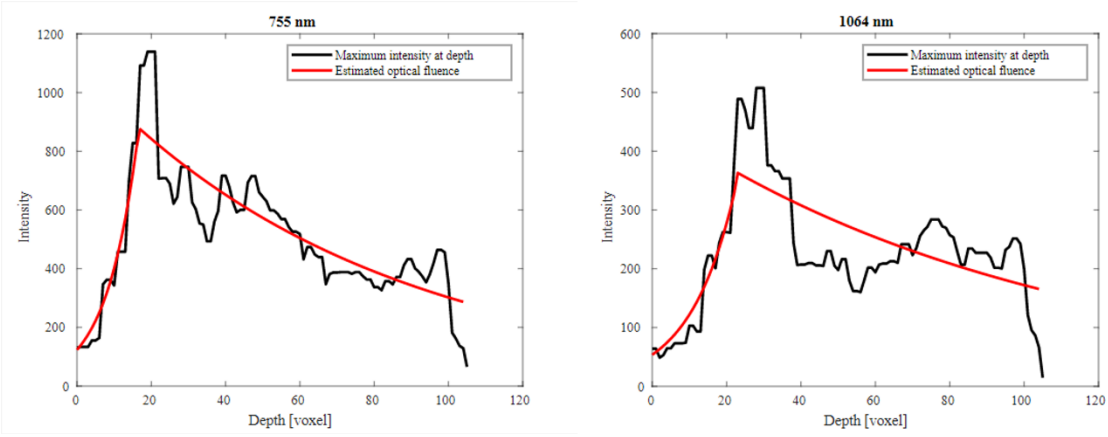

(a) (b)

Figure 33: Maximum voxel brightness (black) as a function of depth through the mouse with a voxel size of 0.1mm. Average estimated exponential curves of the optical fluence attenuation are in red for (a) 757 nm, measured μ_{eff}=1.26 cm^{-1} and (b) 1064 nm, measured μ_{eff}=0.97 cm^{-1}.

Figures 34 and 35 depict three orthogonal maximum intensity projections of three-dimensional optoacoustic images of a live mouse body acquired with illumination at 755

nm and 1064 nm respectively. The images are color-coded to represent the depth of tissue structures and blood vessels depicted on the images. The top 3 images on both figures were made from original tomographic images before normalization of the optical fluence. The middle 3 images were made after the incident optical fluence normalization through the skin layer of tissue volumes. After the incident optical fluence normalization in the skin layer, one can better see areas of the skin illuminated with lower optical fluence below the abdomen. The bottom 3 images were made after the optical fluence normalization through the depth of tissue volumes. One can recognize the gradual improvement of image quality and quantitative accuracy. The major vasculature of the mouse in the very center of the mouse body is resolved and well contrasted after application of the optical fluence normalization through the depth of tissues in the entire volume of interest.

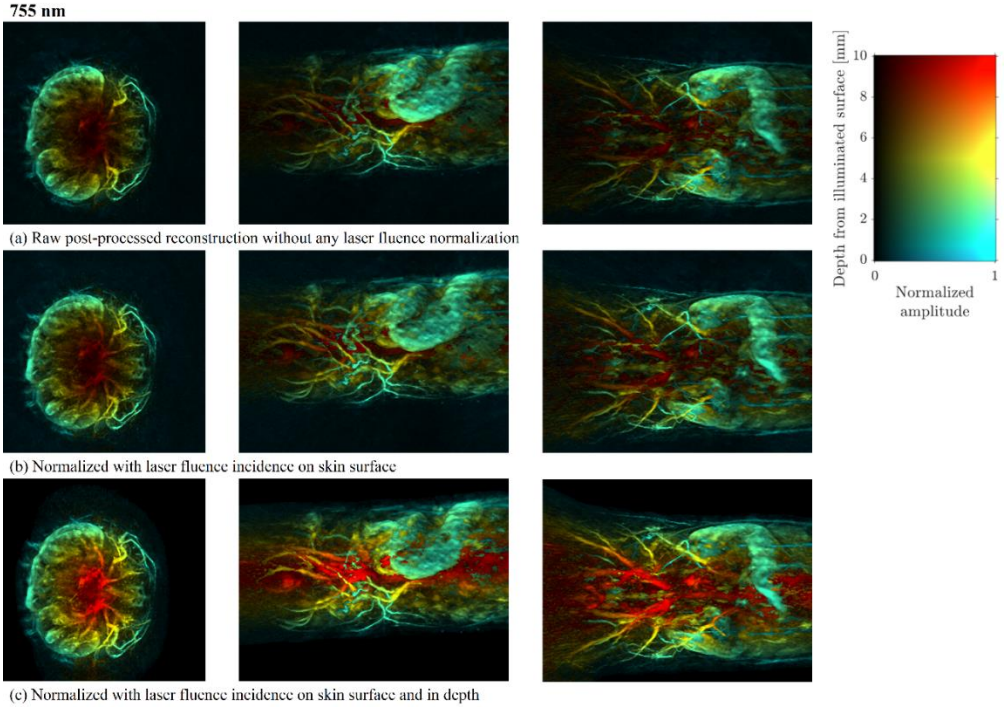

Figure 34: Maximum intensity projection of the mouse with 755 nm wavelength from (a) 3D OAT to (b) compensation of incident fluence on the skin to finally (c) compensation of incident fluence and in-depth through the mouse

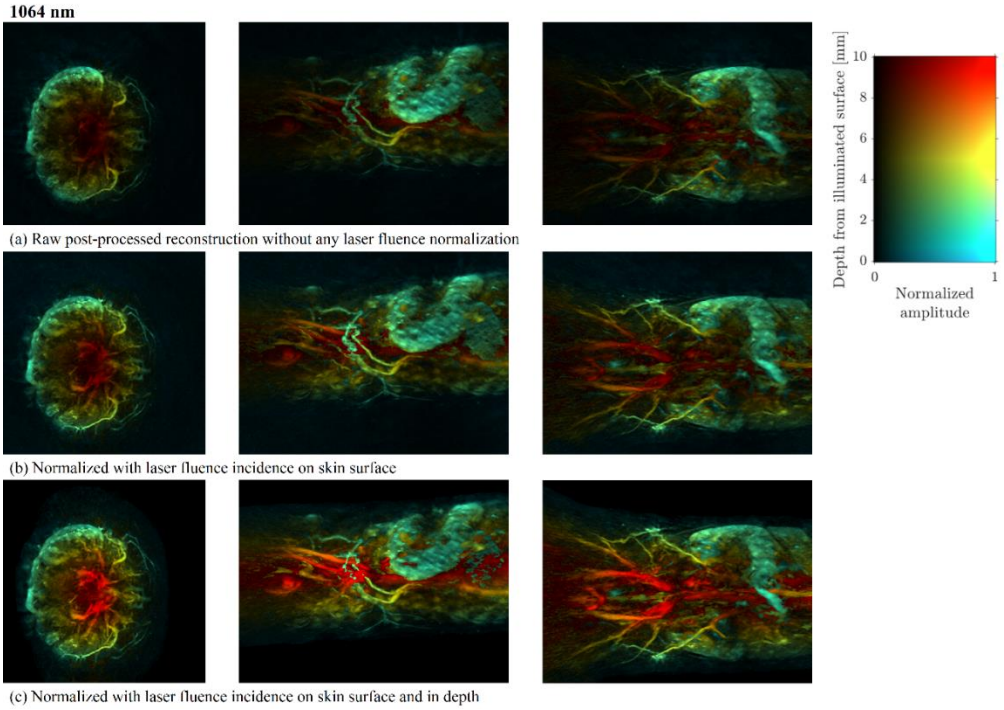

Figure 35: Maximum intensity projection of the mouse with 1064 nm wavelength from (a) 3D OAT to (b) compensation of incident fluence on the skin to finally (c) compensation of incident fluence and in-depth through the mouse

The third step is the optical fluence calibration between the two wavelengths used to calculate functional images from measured optoacoustic images. To determine the ratio of the incident laser fluence at the wavelengths of 1064 and 755 nm, we used the brightness of voxels that belong to arteries. Since all arteries are assumed to have the same blood oxygen saturation of 100%, their optical absorption coefficient is equal through the volume of interest. We acquired two co-registered images at the wavelengths of 1064 and 755 nm. While the 1064 nm wavelength from the Nd:YAG laser had originally more energy compared to the 755 nm wavelength from the OPO laser, it was strongly attenuated by the water of the optoacoustic coupling liquid. To compensate for the difference in the incident optical fluence at two different wavelengths, the mean brightness from the same segment of an artery visible on both 3D images was compared. The artery chosen is the aorta

positioned close to the spinal cord and being the smaller blood vessel as compared to its neighboring vein. We were assured in our choice of this artery by observing that at 1064 nm this artery possessed a higher mean brightness compared with the larger neighboring vein, while the ratio of brightness of the two blood vessels was inverted on the optoacoustic image acquired at 755 nm. This observation corresponds to the optical absorption ratio between arteries and veins [79].

The ratio of the optical absorption at 1064 nm and 755 nm for arterial blood with 100% oxygenation equals 1.16. The measured ratio of the artery on the experimentally acquired images was 0.73. As a result of comparative brightness analysis in the 3D images of the same artery acquired with two laser wavelengths, we determined that a multiplication coefficient of 1.6 is required for the image acquired at 1064 nm to be calibrated to the image acquired at 755 nm. The original segmented aorta image brightness between 1064 and 755 nm wavelengths with expected ratio and resultant brightness after calibration between wavelengths can be seen in Table 9. Figure 36 shows two pairs of optoacoustic image slices before and after the multiplier was applied. After the optical fluence calibration between the two wavelengths, the brightness of the two co-registered optoacoustic images has become proportional to the optical absorption coefficient. From that point, the two quantitative optoacoustic images could be used for the generation of functional images with brightness proportional to the total hemoglobin [tHb] and of blood oxygen saturation [sO_2].

Table 9: Mean OAT aorta value from a single slice after laser fluence equalization at the individual wavelengths of 755 and 1064 nm. 1.6 multiplier was applied to the 1064nm wavelength based on the estimated absorption values of sO_2=100% sO_2 to achieve the expected ratio.

	Aorta		
	755 nm	1064 nm	Ratio
OAT	393.05	287.57	1.37
μ_a	7.51	8.7	0.86
Norm. OAT	393.05	458.11	0.86

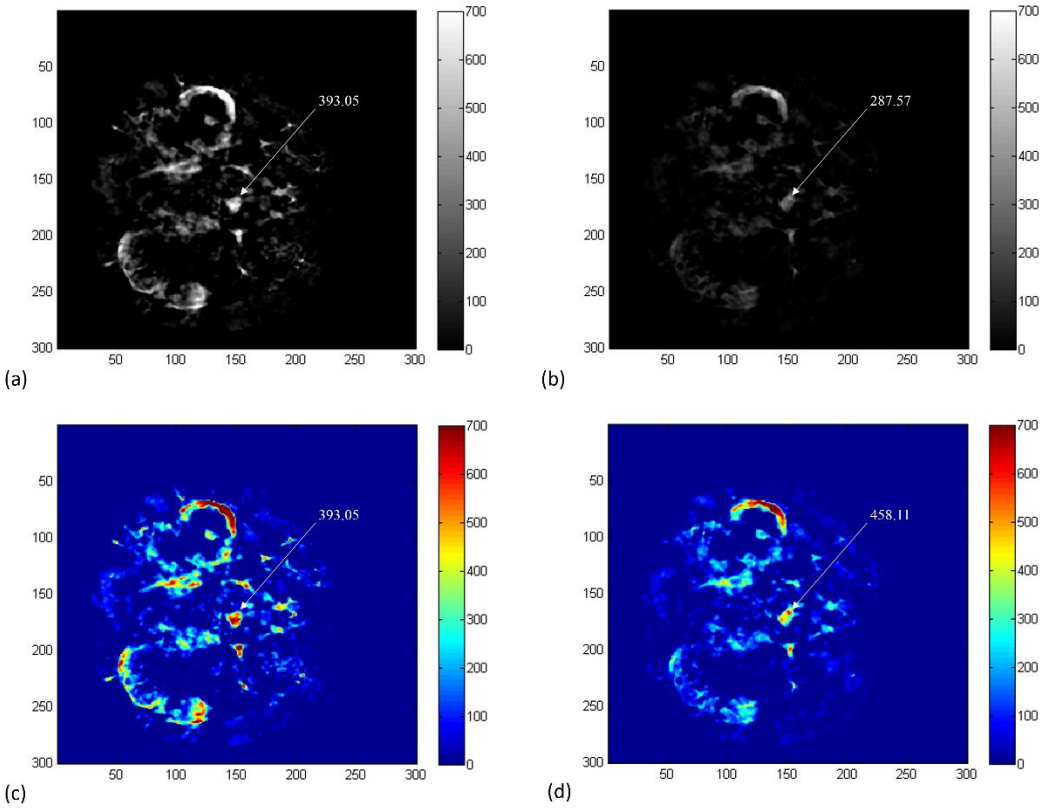

Figure 36: Calibration of the 755 and 1064 nm wavelengths with (a) showing the 755 nm wavelength; (b) the 1064 nm wavelength with no multi-wavelength calibration; (c) the same 755 nm wavelength but in color; (d) the 1064 nm volume after wavelength calibration in color.

To estimate the accuracy of our method for optical fluence equalization on the surface, normalization through the depth and calibration between two laser wavelengths, we compared the brightness of arteries as visualized in a volume of live tissue. Different

arteries were segmented at different depths in the image volume, and their brightness was measured. We compared the differences in arterial brightness prior to and after the optical fluence normalization. The data is presented in Table 10. Even though the optical absorption coefficient of arterial blood is constant through the volume, the brightness of arteries varies due to the variations of their diameters. When normalized to diameter the brightness of arteries after the optical fluence normalization has become approximately equal with an error of 11% from the maximum artery value which is an improvement of about 5% from pre-normalization.

Table 10: Various arteries at different depths and heights

		Aorta		Closer to skin		Front Right		
		755 nm	1064 nm	755 nm	1064 nm	755 nm	1064 nm	Average
PreNorm	Mean	176.66	138.59	234.39	149.35	207.35	185.52	
	Median	174.14	133.73	246.84	157.99	192.95	184.46	
	Std Dev	65.54	47.69	93.92	61.63	71.27	51.32	
	% Diff	-0.2945	-0.275	0	-0.1435	-0.2183	0	-0.1552
PostNorm	Mean	610.94	796.78	474.98	529.05	481.50	606.53	
	Median	595.74	764.67	497.31	562.95	454.39	589.67	
	Std Dev	237.57	283.99	192.62	218.72	165.51	177.85	
	% Diff	0	0	-0.1652	-0.2638	-0.2373	-0.0102	-0.1127

5-3: Functional images of [tHb] and [sO_2]

Figure 37 is a summation of 755 and 1064 nm wavelengths which provides a proportional estimate of total hemoglobin (see Equation 16). Due to the high spatial co-registration of the optoacoustic images acquired at two wavelengths, the shape of blood vessels and organs are maintained on the [tHb] image with high spatial resolution.

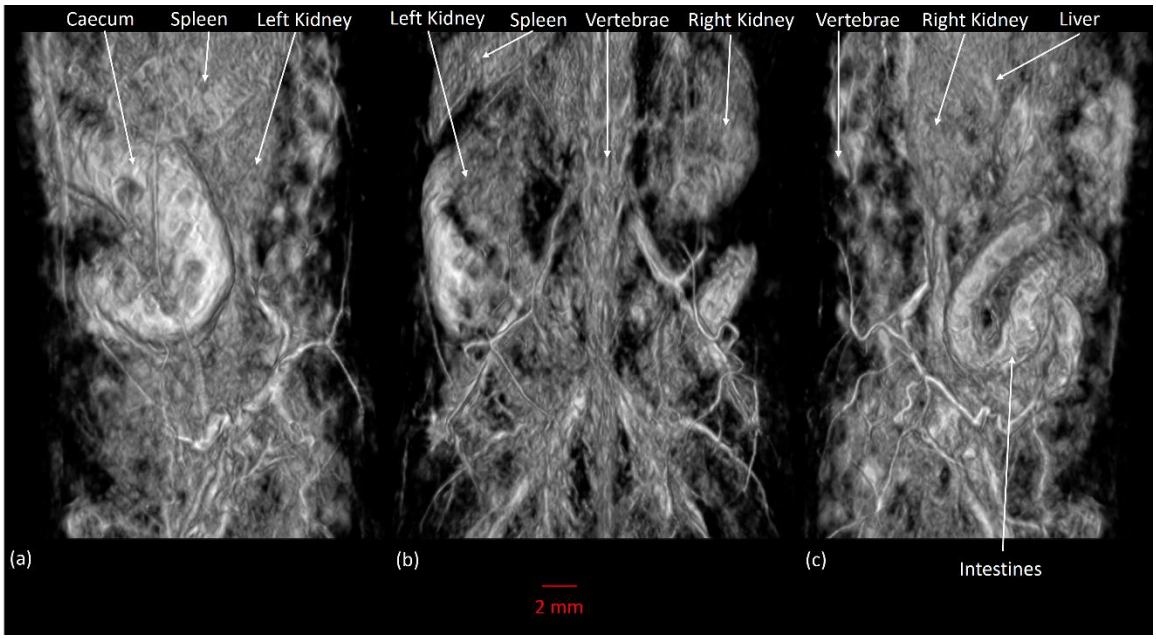

Figure 37: Total hemoglobin volume after optical fluence normalization through the volume of live tissue and voxel brightness normalization between wavelengths. (a) is the left side of the mouse, (b) is the backside of the mouse, and (c) is the right side of the mouse.

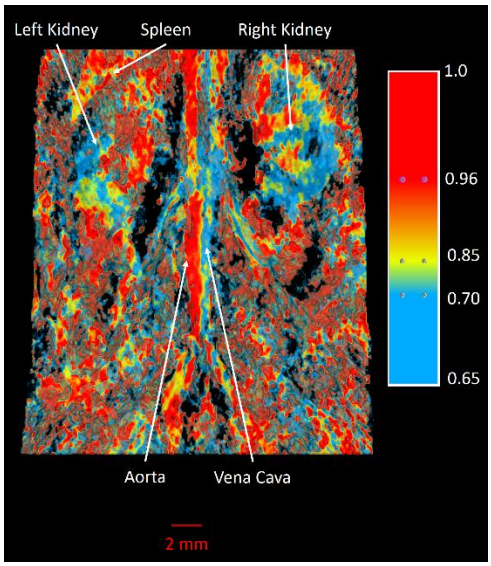

Figure 38: Functional optoacoustic imaging of the lower mouse body separating aorta and vena cava with intermediate blood oxygen saturation of yellow in-between.

Figure 38 depicts the first experimentally obtained volumetric 3D functional image of blood oxygen saturation generated by qOAT system based on two optoacoustic images acquired at 757 nm and 1064 nm wavelengths after the full process of optical fluence

equalization on the skin, normalization through the depth of the entire volume of tissues and calibration between two different wavelengths. The functional image of [sO_2] is visualized to display three ranges of blood oxygenation: (i) 100% to 96% - arterial blood, (ii) 96% to 70% - organs and other tissue structures, and (iii) 70% to 65% - veins with the lowest blood oxygen saturation.

Due to the procedure of division between two images, the noise on the resulting [sO_2] image is significant. On the other hand, the [sO_2] image separates arteries, veins and tissues with intermediate oxygenation.

5-4: Conclusion

In this study, we measured the distribution of the absorbed optical energy as a function of depth from three-dimensional optoacoustic images of heterogeneous live tissues, and thereby determined the average optical attenuation coefficient. These measurements were made possible by the presence of background tissue information on raw unprocessed optoacoustic images, which in turn was enabled by the presence of low-frequency sensitivity of the ultrawide-band ultrasonic transducers. Unlike common transducers made for ultrasound imaging with a bandwidth of 50-80% extending into high frequencies for purposes of higher spatial resolution, our transducers and analog electronics were designed to provide high resolution and simultaneously keep the low-frequency components to provide volumetric information and quantitative accuracy.

Analysis of the curves of the effective optical attenuation depicted in Figure 33 were measured to become an average optical attenuation coefficient which can be used as the first approximation to the problem of the optical fluence normalization through the

volume of live tissues. This in turn enables the possibility for functional imaging of blood oxygen saturation. In this work, we report a volumetric 3D functional image of blood oxygen saturation in a live mouse that shows the separation of arteries, veins, and tissues based on images of the optical absorption coefficient acquired at two different laser wavelengths.

CHAPTER 6: CONCLUSION

The LOIS-3D system was developed for preclinical research applications in small animal models. The noise effective pressure was measured to be ~1.9 Pa when not averaging with a system sensitivity around 4.7 mV/Pa. LOIS-3D has an improved resolution of 0.14 mm and sensitivity of 0.15 cm^{-1} with the possibility of even better sensitivity with laser power that is closer to the ANSI limit which would be around 0.03 cm^{-1}. Comparisons to other commercially available systems [58] showed that the LOIS-3D had three times better sensitivity. Even in very sensitive areas such as molecular imaging where the concentrations of molecules can be in the pmol/mL range, the system was able to detect this range in an optically scattering phantom simulating low blood surroundings. Several studies were done to show the capability of the LOIS-3D system ranging from improvements in the quantitative image through compensation of light attenuation in-depth, to the kinetics of gold nanorods and tracking deposition of targeted IR800dye on the tumor.

The major scientific contribution is to the improved accuracy of the distribution of absorbed optical energy. Each wavelength scan would undergo equalization of optical fluence on the skin surface and then normalization through the depth of volume of live tissue based on experimental measurement of the voxel brightness using experimentally acquired and reconstructed images. Owing to our unique ultrasonic transducers sensitive within ultrawideband of ultrasonic frequencies from 50 kHz to 8MHz, the exponential trend of the effective optical attenuation as a function of depth has been measured from blood vessels having constant optical absorption. The method produced more accurate quantitative images of the optical absorption coefficient in live animals compared with

methods of the optical fluence normalization based on computational forward models of light propagation in tissues with *a priori* unknown optical properties.

Quantitative image calibration has been developed based on a comparison of the voxel brightness of an artery (a strongly absorbing vessel with well-defined blood oxygen saturation of 100%) visualized with two different illumination wavelengths. Previously unattainable 3D functional images of [tHb] and [sO2] in live mouse tissues have been reconstructed using two spatially co-registered images acquired using illumination wavelengths of 755nm and 1064nm at which the ratio of [Hb] and [HbO2] optical absorption coefficients are inverted. The accuracy of functional images has been validated qualitatively by our capability to separate arteries, veins, and organs nearby each other through the entire volume of functional images, and quantitatively by comparison of arterial brightness at different depths of a mouse body.

Here we report the first experimentally obtained volumetric 3D functional image of blood oxygen saturation generated by LOIS-3D system based on two optoacoustic images acquired at 757 nm and 1064 nm wavelengths after the full process of optical fluence equalization on the skin, normalization through the depth of the entire volume of tissues and calibration between two different wavelengths. This image the shows separation of arteries, veins, and tissues based on images of the optical absorption coefficient.

REFERENCES

1. Oraevsky, A.A., Jacques, S.L., Esenaliev, R.O., Tittel, F.K., *Laser based optoacoustic imaging in biological tissues.* Proc. SPIE, 1994. **2134A**: p. 122-128.
2. Oraevsky, A.A., Jacques, S.L., Esenaliev, R.O., Tittel, F.K., ed. *Time-resolved optoacoustic imaging in layered biological tissues*. Advances in Optical Imaging and Photon Migration, ed. R.R. Alfano. Vol. 21. 1994, OSA Publishing House: Washington, DC. p. 161-165.
3. Kruger, R.A., Liu, P., *Photoacoustic ultrasound: Theory.* Proc. SPIE, 1994. **2134A**: p. 114-118.
4. Kruger, R.A., Liu, P., *Photoacoustic ultrasound: experimental results.* Proc. SPIE, 1994. **2134A**: p. 114-118.
5. Wang, L.V., *Tutorial on Photoacoustic Microscopy and Computed Tomography.* IEEE Journal of Selected Topics in Quantum Electronics, 2008. **14**(1): p. 171-179.
6. Oraevsky, A.A. and A.A. Karabutov, *Optoacoustic Tomography* in Biomedical Photonics Handbook, T. Vo-Dinh, Editor. CRC Press: Boca Raton - London - New York - Washington, DC., 2003: p. 34/1-34/34.
7. Oraevsky, A.A., *Optoacoustics Tomography: From Fundamentals to Diagnostic Imaging of Breast Cancer*, in *Biomedical Photonics Handbook*, T. Vo-Dinh, Editor. 2014, CRC Press: Boca Raton, Florida. p. 715-751.
8. Andreev, V.G., A.A. Karabutov, S.V. Solomatin, E.A. Savateeva, L.V. Aleynikov, Y.V. Zhulina, D.R. Fleming, and A.A. Oraevsky, *Optoacoustic tomography of breast cancer with arc-array transducer.* Proceedings SPIE, 2000. **3916**: p. 36-47.

9. Wang, K., S.A. Ermilov, R. Su, H.P. Brecht, A.A. Oraevsky, and M.A. Anastasio, *An imaging model incorporating ultrasonic transducer properties for three-dimensional optoacoustic tomography.* IEEE Trans Med Imaging, 2011. **30**(2): p. 203-14.

10. Rosenthal, A., V. Ntziachristos, and D. Razansky, *Model-based optoacoustic inversion with arbitrary-shape detectors.* Med Phys, 2011. **38**(7): p. 4285-95.

11. Wang, K., R. Su, A.A. Oraevsky, and M.A. Anastasio, *Investigation of iterative image reconstruction in three-dimensional optoacoustic tomography.* Phys Med Biol, 2012. **57**(17): p. 5399-423.

12. Wang, K. and M.A. Anastasio, *Photoacoustic and Thermoacoustic Tomography: Image Formation Principles*, in *Handbook of Mathematical Methods in Imaging*, O. Scherzer, Editor. 2011, Springer New York: New York, NY. p. 781-815.

13. Goldschmidt, B.S., S. Mehta, J. Mosley, C. Walter, P.J. Whiteside, H.K. Hunt, and J.A. Viator, *Photoacoustic measurement of refractive index of dye solutions and myoglobin for biosensing applications.* Biomed Opt Express, 2013. **4**(11): p. 2463-76.

14. Zhou, Y., G. Li, L. Zhu, C. Li, L.A. Cornelius, and L.V. Wang, *Handheld photoacoustic probe to detect both melanoma depth and volume at high speed in vivo.* Journal of Biophotonics, 2015. **8**(11-12): p. 961-967.

15. Staley, J., P. Grogan, A.K. Samadi, H. Cui, M.S. Cohen, and X. Yang, *Growth of melanoma brain tumors monitored by photoacoustic microscopy.* J Biomed Opt, 2010. **15**(4): p. 040510.

16. Zhou, Y., W. Xing, K.I. Maslov, L.A. Cornelius, and L.V. Wang, *Handheld photoacoustic microscopy to detect melanoma depth in vivo.* Opt Lett, 2014. **39**(16): p. 4731-4.

17. Welch, A.J. and M.C. van Gemert, *Optical-Thermal Response of Laser-Irradiated Tissue.* 1995.

18. Wang, X., Y. Pang, G. Ku, X. Xie, G. Stoica, and L.V. Wang, *Noninvasive laser-induced photoacoustic tomography for structural and functional in vivo imaging of the brain.* Nat Biotechnol, 2003. **21**(7): p. 803-6.

19. Ntziachristos, V. and D. Razansky, *Molecular imaging by means of multispectral optoacoustic tomography (MSOT).* Chem Rev, 2010. **110**(5): p. 2783-94.

20. Beard, P., *Biomedical photoacoustic imaging.* Interface Focus, 2011. **1**: p. 602–631.

21. Luke, G.P., D. Yeager, and S.Y. Emelianov, *Biomedical applications of photoacoustic imaging with exogenous contrast agents.* Ann Biomed Eng, 2012. **40**(2): p. 422-37.

22. Wang, L.V. and S. Hu, *Photoacoustic tomography: in vivo imaging from organelles to organs.* Science, 2012. **335**(6075): p. 1458-1462.

23. Oraevsky, A.A., B. Clingman, J. Zalev, A.T. Stavros, W.T. Yang, and J.R. Parikh, *Clinical optoacoustic imaging combined with ultrasound for coregistered functional and anatomical mapping of breast tumors.* Photoacoustics, 2018. **12**: p. 30-45.

24. Lin, L., P. Hu, J. Shi, C.M. Appleton, K. Maslov, L. Li, R. Zhang, and L.V. Wang, *Single-breath-hold photoacoustic computed tomography of the breast.* Nat Commun, 2018. **9**(1): p. 2352.

25. Toi, M., Y. Asao, Y. Matsumoto, H. Sekiguchi, A. Yoshikawa, M. Takada, M. Kataoka, T. Endo, N. Kawaguchi-Sakita, M. Kawashima, E. Fakhrejahani, S. Kanao, I. Yamaga, Y. Nakayama, M. Tokiwa, M. Torii, T. Yagi, T. Sakurai, K. Togashi, and T. Shiina, *Visualization of tumor-related blood vessels in human breast by photoacoustic imaging system with a hemispherical detector array.* Sci Rep, 2017. **7**: p. 41970.

26. Knieling, F., C. Neufert, A. Hartmann, J. Claussen, A. Urich, C. Egger, M. Vetter, S. Fischer, L. Pfeifer, A. Hagel, C. Kielisch, R.S. Gortz, D. Wildner, M. Engel, J. Rother, W. Uter, J. Siebler, R. Atreya, W. Rascher, D. Strobel, M.F. Neurath, and M.J. Waldner, *Multispectral Optoacoustic Tomography for Assessment of Crohn's Disease Activity.* N Engl J Med, 2017. **376**(13): p. 1292-1294.

27. Seno Medical Instruments, I., *Imagio Breast Imaging System*. FDA.

28. Cox, B., J.G. Laufer, S.R. Arridge, and P.C. Beard, *Quantitative spectroscopic photoacoustic imaging: a review.* J Biomed Opt, 2012. **17**(6): p. 061202.

29. Dean-Ben, X.L., S. Gottschalk, B. Mc Larney, S. Shoham, and D. Razansky, *Advanced optoacoustic methods for multiscale imaging of in vivo dynamics.* Chem Soc Rev, 2017. **46**(8): p. 2158-2198.

30. Attia, A.B.E., G. Balasundaram, M. Moothanchery, U.S. Dinish, R. Bi, V. Ntziachristos, and M. Olivo, *A review of clinical photoacoustic imaging: Current and future trends.* Photoacoustics, 2019. **16**: p. 100144.

31. Heywang-Kobrunner, S.H., A. Hacker, and S. Sedlacek, *Advantages and Disadvantages of Mammography Screening.* Breast Care (Basel), 2011. **6**(3): p. 199-207.

32. Administration, U.S.F.D. *MRI Benefits and Risks*. 2017 [cited 2021 May 22]; Available from: https://www.fda.gov/radiation-emitting-products/mri-magnetic-resonance-imaging/benefits-and-risks.

33. Liopo, A.V., R. Su, and A.A. Oraevsky, *Melanin nanoparticles as a novel contrast agent for optoacoustic tomography.* Photoacoustics, 2015. **3**: p. 35-43.

34. Longo, D.L., R. Stefania, S. Aime, and A. Oraevsky, *Melanin-Based Contrast Agents for Biomedical Optoacoustic Imaging and Theranostic Applications.* Int J Mol Sci, 2017. **18**(8).

35. de la Zerda, A., J.W. Kim, E.I. Galanzha, S.S. Gambhir, and V.P. Zharov, *Advanced contrast nanoagents for photoacoustic molecular imaging, cytometry, blood test and photothermal theranostics.* Contrast Media Mol Imaging, 2011. **6**(5): p. 346-69.

36. Tsyboulski, D.A., A.V. Liopo, R. Su, S.A. Ermilov, S. Bachilo, R.B. Weiman, and A.A. Oraevsky, *Enabling in vivo measurements of nanoparticles concentrations with three-dimensional optoacoustic tomography* J. Biophotonics 2014. **7**(8): p. 581-588.

37. Li, W., P.K. Brown, L.V. Wang, and Y. Xia, *Gold nanocages as contrast agents for photoacoustic imaging.* Contrast Media Mol Imaging, 2011. **6**(5): p. 370-7.

38. Pan, D., M. Pramanik, S.A. Wickline, L.V. Wang, and G.M. Lanza, *Recent advances in colloidal gold nanobeacons for molecular photoacoustic imaging.* Contrast Media Mol Imaging, 2011. **6**(5): p. 378-88.

39. Su, R., S.A. Ermilov, A.V. Liopo, and A.A. Oraevsky, *Three-dimensional optoacoustic imaging as a new noninvasive technique to study long-term biodistribution of optical contrast agents in small animal models.* J Biomed Opt, 2012. **17**(10): p. 101506.

40. Chen, Z., X.L. Dean-Ben, S. Gottschalk, and D. Razansky, *Performance of optoacoustic and fluorescence imaging in detecting deep-seated fluorescent agents.* Biomed Opt Express, 2018. **9**(5): p. 2229-2239.

41. Garcia-Allende, P.B., J. Glatz, M. Koch, and V. Ntziachristos, *Enriching the interventional vision of cancer with fluorescence and optoacoustic imaging.* J Nucl Med, 2013. **54**(5): p. 664-7.

42. Zhou, Y., J. Yao, and L.V. Wang, *Tutorial on photoacoustic tomography.* J Biomed Opt, 2016. **21**(6): p. 61007.

43. Brecht, H.P., R. Su, M. Fronheiser, S.A. Ermilov, A. Conjusteau, and A.A. Oraevsky, *Whole-body three-dimensional optoacoustic tomography system for small animals.* J Biomed Opt, 2009. **14**(6): p. 064007.

44. Esenaliev, R.O., *Optoacoustic Monitoring of Physiologic Variables.* Front Physiol, 2017. **8**: p. 1030.

45. Perekatova, V., P. Subochev, M. Kleshnin, and I. Turchin, *Optimal wavelengths for optoacoustic measurements of blood oxygen saturation in biological tissues.* Biomed Opt Express, 2016. **7**(10): p. 3979-3995.

46. Maslov, K., G. Stoica, and L.V. Wang, *In vivo dark-field reflection-mode photoacoustic microscopy.* Opt Lett, 2005. **30**(6): p. 625-7.

47. Wang, X., Y. Pang, G. Ku, G. Stoica, and L.V. Wang, *Three-dimensional laser-induced photoacoustic tomography of mouse brain with the skin and skull intact.* Opt Lett, 2003. **28**(19): p. 1739-41.

48. Zhang, E.Z., J.G. Laufer, R.B. Pedley, and P.C. Beard, *In vivo high-resolution 3D photoacoustic imaging of superficial vascular anatomy.* Phys Med Biol, 2009. **54**(4): p. 1035-46.

49. Fronheiser, M.P., S.A. Ermilov, H.P. Brecht, A. Conjusteau, R. Su, K. Mehta, and A.A. Oraevsky, *Real-time optoacoustic monitoring and three-dimensional mapping of a human arm vasculature.* J Biomed Opt, 2010. **15**(2): p. 021305.

50. Bilaniuk, N. and G.S.K. Wong, *Speed of sound in pure water as a function of temperature.* The Journal of the Acoustical Society of America, 1993. **93**(3): p. 1609-1612.

51. Lassen, M., *An Introduction to the Physics of Diagnostic Radiology, by E. E. Christensen, T. S. Curry III, and J. E. Dowdey.* Medical Physics, 1980. **7**(3): p. 268-270.

52. ANSI, *Americal National Standard for Safe Use of Lasers.* Americal National Standards Institutes, 2007. **Z136.1**: p. 6-24.

53. Conjusteau, A., S.A. Ermilov, R. Su, H.P. Brecht, M.P. Fronheiser, and A.A. Oraevsky, *Measurement of the spectral directivity of optoacoustic and ultrasonic transducers with a laser ultrasonic source.* Rev Sci Instrum, 2009. **80**(9): p. 093708.

54. Jolliffe, I.T. and J. Cadima, *Principal component analysis: a review and recent developments.* Philos Trans A Math Phys Eng Sci, 2016. **374**(2065): p. 20150202.

55. Xu, M. and L.V. Wang, *Universal back-projection algorithm for photoacoustic computed tomography.* Phys Rev E Stat Nonlin Soft Matter Phys, 2005. **71**(1 Pt 2): p. 016706.

56. Karabutov, A.A., E.V. Savateeva, N.B. Podymova, and A.A. Oraevsky, *Backward mode detection of laser-induced wide-band ultrasonic transients with optoacoustic transducer.* Journal of Applied Physics, 2000. **87**(4): p. 2003-2014.

57. Wang, K., C. Huang, Y.J. Kao, C.Y. Chou, A.A. Oraevsky, and M.A. Anastasio, *Accelerating image reconstruction in three-dimensional optoacoustic tomography on graphics processing units.* Med Phys, 2013. **40**(2): p. 023301.

58. Joseph, J., M.R. Tomaszewski, I. Quiros-Gonzalez, J. Weber, J. Brunker, and S.E. Bohndiek, *Evaluation of Precision in Optoacoustic Tomography for Preclinical Imaging in Living Subjects.* J Nucl Med, 2017. **58**(5): p. 807-814.

59. Oraevsky, A.A., Oraevsky, A.N., *Plasmon resonance in ellipsoid nanoparticles.* Quantum Electronics, 2002. **32**(1): p. 79-82.

60. James, M.L. and S.S. Gambhir, *A molecular imaging primer: modalities, imaging agents, and applications.* Physiol Rev, 2012. **92**(2): p. 897-965.

61. Weber, J., P.C. Beard, and S.E. Bohndiek, *Contrast agents for molecular photoacoustic imaging.* Nat Methods, 2016. **13**(8): p. 639-50.

62. Institute, N.H.G.R. *Why Mouse Matters*. 2010 [cited 2020 January 13]; Available from: https://www.genome.gov/10001345/importance-of-mouse-

genome#:~:text=On%20average%2C%20the%20protein%2Dcoding,are%20only%2060%20percent%20identical.

63. Iwaki, T., H. Yamashita, and T. Hayakawa, *Heads and Faces in: A Color Atlas of Sectional Anatomy of the Mouse*. 2005, Tokyo, Japan: Maruzen Publishing Co.

64. Liopo, A.V., A. Conjusteau, O.V. Chumakova, S.A. Ermilov, R. Su, and A.A. Oraevsky, *Highly purified biocompatible gold nanorods for contrasted optoacoustic imaging of small animal models.* Nanosci Nanotechnol Lett, 2012. **4**(7): p. 681-686.

65. Liopo, A., A. Conjusteau, M. Konopleva, M. Andreeff, and A. Oraevsky, *Photothermal therapy of acute leukemia cells in the near-infrared region using gold nanorods CD-33 conjugates*. SPIE BiOS. Vol. 7897. 2011: SPIE.

66. Tong, L., Q. Wei, A. Wei, and J.X. Cheng, *Gold nanorods as contrast agents for biological imaging: optical properties, surface conjugation and photothermal effects.* Photochem Photobiol, 2009. **85**(1): p. 21-32.

67. Cho, W.S., M. Cho, J. Jeong, M. Choi, H.Y. Cho, B.S. Han, S.H. Kim, H.O. Kim, Y.T. Lim, B.H. Chung, and J. Jeong, *Acute toxicity and pharmacokinetics of 13 nm-sized PEG-coated gold nanoparticles.* Toxicol Appl Pharmacol, 2009. **236**(1): p. 16-24.

68. von Maltzahn, G., J.H. Park, A. Agrawal, N.K. Bandaru, S.K. Das, M.J. Sailor, and S.N. Bhatia, *Computationally guided photothermal tumor therapy using long-circulating gold nanorod antennas.* Cancer Res, 2009. **69**(9): p. 3892-900.

69. Oraevsky, A., *Gold and silver nanoparticles as contrast agents for optoacoustic imaging*, in *Photoacoustic imaging and spectroscopy*, L. Wang, Editor. 2009, Taylor and Francis Group: New York.

70. Eghtedari, M., A.V. Liopo, J.A. Copland, A.A. Oraevsky, and M. Motamedi, *Engineering of hetero-functional gold nanorods for the in vivo molecular targeting of breast cancer cells.* Nano Lett, 2009. **9**(1): p. 287-91.

71. de Freitas, L.F. and M.R. Hamblin, *Proposed Mechanisms of Photobiomodulation or Low-Level Light Therapy.* IEEE J Sel Top Quantum Electron, 2016. **22**(3).

72. Niidome, T., M. Yamagata, Y. Okamoto, Y. Akiyama, H. Takahashi, T. Kawano, Y. Katayama, and Y. Niidome, *PEG-modified gold nanorods with a stealth character for in vivo applications.* J Control Release, 2006. **114**(3): p. 343-347.

73. Lankveld, D.P., R.G. Rayavarapu, P. Krystek, A.G. Oomen, H.W. Verharen, T.G. van Leeuwen, W.H. De Jong, and S. Manohar, *Blood clearance and tissue distribution of PEGylated and non-PEGylated gold nanorods after intravenous administration in rats.* Nanomedicine (Lond), 2011. **6**(2): p. 339-49.

74. Carr, J. *New Imaging Agent Enables Better Cancer Detection, More Accurate Staging, Drug Designed and Developed at UC San Diego School of Medicine*. 2013 [cited 2021 February 18]; Available from: https://ucsdnews.ucsd.edu/pressrelease/new_imaging_agent_enables_better_cancer_detection_more_accurate_staging.

75. Qin, Z., D.J. Hall, M.A. Liss, C.K. Hoh, C.J. Kane, A.M. Wallace, and D.R. Vera, *Optimization via specific fluorescence brightness of a receptor-targeted probe for*

optical imaging and positron emission tomography of sentinel lymph nodes. J Biomed Opt, 2013. **18**(10): p. 101315.

76. Jacques, S.L., *Optical properties of biological tissues: a review.* Phys Med Biol, 2013. **58**(11): p. R37-61.

77. Dean-Ben, X.L., G. Sela, A. Lauri, M. Kneipp, V. Ntziachristos, G.G. Westmeyer, S. Shoham, and D. Razansky, *Functional optoacoustic neuro-tomography for scalable whole-brain monitoring of calcium indicators.* Light Sci Appl, 2016. **5**(12): p. e16201.

78. Zhang, P., L. Li, L. Lin, P. Hu, J. Shi, Y. He, L. Zhu, Y. Zhou, and L.V. Wang, *High-resolution deep functional imaging of the whole mouse brain by photoacoustic computed tomography in vivo.* J Biophotonics, 2018. **11**(1).

79. Roggan, A., M. Friebel, K. Do Rschel, A. Hahn, and G. Mu Ller, *Optical Properties of Circulating Human Blood in the Wavelength Range 400-2500 nm.* J Biomed Opt, 1999. **4**(1): p. 36-46.

80. Prahl, S. *Optical absorption of hemoglobin*. 1998; http://omlc.ogi.edu/spectra/hemoglobin/].

81. Petrova, E.V., S.A. Ermilov, R. Su, V. Nadvoretsky, A. Conjusteau, and A.A. Oraevsky, *Using optoacoustic imaging for measuring the temperature dependence of Grüneisen parameter in optically absorbing solutions.* Opt Exp, 2013. **21**(21): p. 25077-25090.

82. Hochuli, R., S. Powell, S. Arridge, and B. Cox, *Quantitative photoacoustic tomography using forward and adjoint Monte Carlo models of radiance.* Journal of Biomedical Optics, 2016. **21**(12): p. 126004.

APPENDIX: SUMMARY OF SCIENTIFIC ACCOMPLISHMENTS

Improvements to science ranged from helping determine and specifying parameters useful for quantitatively accurate measurements to testing the system in various applications. Specifically, ensuring that the system was ultrawide band in order to maintain low frequency signals to ensure enough data is acquired for better detection of small and large objects. This would also work in-conjunction to allow a better correction in the deconvolution of acousto-electric impulse response of the signal to allow the reconstruction image to be able to show the optical fluence attenuation which in turn could be used to help get the absolution absorption coefficient which is the goal of optoacoustics in the functional and molecular fields. The sensitivity of the system was tested with various contrast agents and compared to a comparable commercial system in order to prove its capability.

A novel method of optical fluence normalization through the skin surface and through the volume of live tissue based on experimental measurement of the voxel brightness using experimentally acquired and reconstructed images was developed. The exponential trend of the effective optical attenuation as a function of depth was only possible through the use of ultrawide band of ultrasonic frequencies from 50kHz to 8MHz found in our transducers. In addition, a method of quantitative image calibration based on comparing the voxel brightness of an artery (a strongly absorbing vessel with well-defined blood oxygen saturation of 100%) visualized with two different illumination wavelengths. Previously unattainable 3D functional images of [tHb] and [sO2] in live mouse tissues have been reconstructed using two spatially co-registered images acquired using illumination wavelengths of 755nm and 1064nm at which the ratio of [Hb] and [HbO2] optical absorption coefficients is inverted. These methods produced more accurate quantitative

images of the optical absorption coefficient in live animals compared with methods of the optical fluence normalization based on computational forward models of light propagation in tissues with *a priori* unknown optical properties.